

Hamiltonian simulation-based quantum-selected configuration interaction for large-scale electronic structure calculations with a quantum computer

Kenji Sugisaki,^{1,2,3,4,*} Shu Kanno,^{5,1} Toshinari Itoko,^{6,1} Rei Sakuma,^{7,1} and Naoki Yamamoto^{8,1,3}

¹*Quantum Computing Center, Keio University, 3-14-1 Hiyoshi, Kohoku-ku, Yokohama, Kanagawa 223-8522, Japan*

²*Graduate School of Science and Technology, Keio University, 7-1 Shinkawasaki, Saiwai-ku, Kawasaki, Kanagawa 212-0032, Japan*

³*Keio University Sustainable Quantum Artificial Intelligence Center (KSQAIC), Keio University, 2-15-45 Mita, Minato-ku, Tokyo 108-8345, Japan*

⁴*Centre for Quantum Engineering, Research and Education (CQuERE), TCG Centres for Research and Education in Science and Technology (TCG CREST), Sector V, Salt Lake, Kolkata 700091, India*

⁵*Mitsubishi Chemical Corporation, Science & Innovation Center, Yokohama, Kanagawa 227-8502, Japan*

⁶*IBM Quantum, IBM Research–Tokyo, 19-21 Nihonbashi Hakozaki-cho, Chuo-ku, Tokyo 103-8510, Japan*

⁷*Materials Informatics Initiative, RD Technology & Digital Transformation Center,*

JSR Corporation, 3-103-9 Tonomachi, Kawasaki-ku, Kawasaki, Kanagawa 210-0821, Japan

⁸*Department of Applied Physics and Physico-Informatics, Keio University, 3-14-1 Hiyoshi, Kohoku-ku, Yokohama, Kanagawa 223-8522, Japan*

(Dated: April 29, 2025)

Quantum-selected configuration interaction (QSCI) is an approach for quantum chemical calculations using current quantum computers. In conventional QSCI, Slater determinants used for the wave function expansion are sampled by iteratively performing approximate wave function preparation and subsequent measurement in the computational basis, and then the subspace Hamiltonian matrix is diagonalized on a classical computer. In this approach, preparation of a high-quality approximate wave function is necessary to accurately compute total energies. Here we propose a Hamiltonian simulation-based QSCI (HSB-QSCI) to avoid this difficulty, by sampling the Slater determinants from quantum states generated by the real-time evolution of approximate wave functions. We provide numerical simulations for the lowest spin-singlet and triplet states of oligoacenes (benzene, naphthalene, and anthracene), phenylene-1,4-dinitrene, and hexa-1,2,3,4,5-pentaene. We found that the HSB-QSCI is applicable not only to molecules where the Hartree–Fock provides a good approximation of the ground state, but also to strongly correlated systems where preparing a high-quality approximate wave function is hard. Hardware demonstrations of the HSB-QSCI are also reported for carbyne molecules expressed by up to 36 qubits, using an IBM Quantum processor. The HSB-QSCI captures more than 99.75% of the correlation energies in the active space by considering about 1% of all the Slater determinants in 36 qubit systems, illustrating the ability of the proposed method to efficiently consider important electronic configurations.

I. INTRODUCTION

Among the diverse topics in the field of quantum computing, quantum chemical calculations of atoms and molecules have attracted attention as a promising application of quantum computers. A method to perform the full-configuration interaction (full-CI) calculation using the quantum phase estimation (QPE) algorithm was proposed in 2005 [1], and proof-of-principle experiments for the full-CI/STO-3G of the H_2 molecule were reported in 2010 [2, 3]. The quantum circuit for QPE-based full-CI is usually very deep, so highly accurate QPE demonstrations were limited to small models with a few qubits [4–8]. Recently a QPE-type algorithm has been demonstrated in models with up to 33 qubits [9], however, it is still challenging to compute total energies of larger molecules with chemical precision (an error less than $1.0 \text{ kcal mol}^{-1}$) on quantum computers available today.

To reduce the computational load of quantum computers, several quantum–classical hybrid algorithms have been proposed. In 2014, the variational quantum eigensolver (VQE) was proposed for quantum chemical calculations using noisy intermediate-scale quantum (NISQ) [10] devices. In VQE, the quantum state corresponding to an approximate wave function is generated using a parameterized quantum circuit, and the energy expectation value is computed by repeatedly performing state preparation and measurements. The parameters are then optimized to minimize the energy expectation value on a classical computer. These steps are iterated until convergence is reached. VQE has been extensively studied both theoretically and experimentally [11], but it often suffers from challenges related to the high sampling cost required to achieve chemical precision [12] and issues with variational optimization in the presence of barren plateaus [13].

As an alternative approach to quantum chemical calculations using current quantum devices, the quantum-selected configuration interaction (QSCI) method has

* ksugisaki@keio.jp

been proposed [14]. In the QSCI, quantum computers are used to sample Slater determinants that are important contributors to the ground state wave function. This can be done by running a quantum circuit to prepare an approximate wave function and measuring the quantum state in the computational basis. The subspace Hamiltonian matrix is then constructed from the Slater determinants selected via quantum computation and diagonalized on a classical computer. In this approach, the quantum computer is anticipated to efficiently sample a polynomial number of important Slater determinants from an exponentially large Hilbert space, and the nature of the quantum states used for sampling determines the accuracy of the calculation. At the stage of preparing an approximate wave function in QSCI, we may employ VQE or the adiabatic state preparation method [14]. To advance the former technique, combining an adaptive strategy for ansatz construction (ADAPT [15]) to enhance the efficiency of VQE [16], and using a simpler cost function for VQE parameter optimization [17] have also been proposed. However, these approaches may still face challenges in variational optimizations when implemented on quantum hardware. It should also be noted that in the latter approach [17], the VQE wave function with optimized parameters does not necessarily correspond to the minimum with respect to the given Hamiltonian.

Another strategy to prepare the quantum state for QSCI is to perform the coupled cluster singles and doubles (CCSD) calculation on a classical computer and embed the CCSD wave function using the local unitary cluster Jastrow (LUCJ) ansatz [18]. By using the LUCJ ansatz and introducing an error mitigation technique called as a self-consistent configuration recovery (SCCR), which is inspired by the structure of chemistry problems, Robledo-Moreno and coworkers reported the QSCI calculations on the IBM superconducting quantum processor and supercomputer ‘‘Fugaku’’ for the nitrogen molecule (N_2) and the iron-sulfur clusters [2Fe-2S] and [4Fe-4S] with up to 77 qubits [19]. This approach has also been applied to interaction energy [20] and excited state calculations [21, 22]. The combination of the QSCI with density matrix embedding theory has also been reported [23]. While this approach appears to be successful, it is not clear whether it is superior to the method of sampling important Slater determinants from the CCSD wave function on a classical computer.

In this work, we report a Hamiltonian simulation-based quantum state preparation for QSCI (HSB-QSCI), in which important Slater determinants are sampled from the quantum states after the real-time evolutions of initial wave functions [24]. Our proposed approach has several advantages over existing methods: (1) A simple approximate wave function, such as the HF wave function, can be used as the initial wave function, and no variational optimization in VQE is required. (2) Different samples can be obtained by changing the duration of the evolution time. (3) The accuracy of the Hamiltonian simulation does not need to be very high. As

we will show later, the first-order Trotter decomposition with the time length of a single Trotter step $\Delta t = 1$ is sufficient to collect important Slater determinants for the organic molecules under study. In addition, Hamiltonian term truncation based on operator locality in the localized molecular orbital basis can help to reduce the computational cost. (4) Feedback of the QSCI results into quantum computations is possible; that is, Slater determinants found to be important in the QSCI wave function can be added to the initial wave functions. (5) Although short-time evolution can be accurately simulated on a classical computer, long-time evolution poses significant challenges for classical simulation.

Note that methods of sampling basis states for Hamiltonian matrix diagonalization based on Hamiltonian simulation have already been investigated in the framework of quantum Krylov subspace algorithms [25, 26]. Unlike the quantum Krylov method, which computes $H_{kl} = \langle \Phi_k | H | \Phi_l \rangle$ and $S_{kl} = \langle \Phi_k | \Phi_l \rangle$ on a quantum computer by sampling, the HSB-QSCI method requires only measurements in the computational (Pauli-Z) basis and is thus less computationally demanding. Here, $|\Phi_k\rangle = U^k |\Phi_0\rangle$, where $U = e^{-iH\Delta t}$, $|\Phi_0\rangle$ is the initial wave function, and H is the Hamiltonian of the system. In the context of the Monte Carlo simulation, a quantum dynamics Hamiltonian Monte Carlo (qdHMC) method is also proposed [27], in which the proposal step is performed on a quantum computer by sampling after time evolution.

As a proof-of-concept demonstration of the HSB-QSCI method, we performed numerical simulations for the spin-singlet ground (S_0) state and the first excited spin-triplet (T_1) state of oligoacenes [benzene (**1**; 12 qubits), naphthalene (**2**; 20 qubits), and anthracene (**3**; 28 qubits)], phenylene-1,4-dinitrene (**4**; 20 qubits), and hexa-1,2,3,4,5-pentaene (**5**; 20 qubits) in both planar and twisted geometries. Our numerical simulations showed that the HSB-QSCI can calculate the total energy with chemical precision by sampling the Slater determinants with about 10–20 steps of Hamiltonian simulations. We also report hardware demonstrations of the HSB-QSCI for the S_0 and T_1 states of three carbyne (one-dimensional sp-hybridized carbon atom chain) molecules including **5**, octa-1,2,3,4,5,6,7-heptaene (**6**; 28 qubits), and deca-1,2,3,4,5,6,7,8,9-nonaene (**7**; 36 qubits) using an IBM Quantum processor `ibm_kawasaki`, with the aid of matrix product operator (MPO)-based classical compression of the quantum circuit for time evolution. The HSB-QSCI energies calculated on `ibm_kawasaki` agree with the CAS-CI values within 0.6 kcal mol⁻¹ of error in **5**. In **6**, chemical precision for the total energy was not achieved with the real quantum device, but the HSB-QSCI predicted the singlet-triplet energy gap and the energy difference between planar and twisted geometries in chemical precision. The energy difference between planar and twisted geometries in the S_0 state of **7** was also calculated with an error of 0.29 kcal mol⁻¹. In **7**, the HSB-QSCI captures more than 99.75% of correlation en-

ergies by considering only about 1% of all the Slater determinants.

II. THEORY

In the *ab initio* molecular orbital theory, the wave function taking into account the electron correlation is expressed by a linear combination of the Slater determinants as follows:

$$|\Phi\rangle = c_{\text{HF}} |\psi_{\text{HF}}\rangle + \sum_n c_n |\psi_n\rangle. \quad (1)$$

Here, $|\psi_{\text{HF}}\rangle$ is the HF determinant and $|\psi_n\rangle$ are electronically excited determinants from the HF, and c_n are the corresponding expansion coefficients. In the CI method, the number of Slater determinants included in the wave function expansion increases rapidly with the number of molecular orbitals and electrons, and the excitation order. To calculate the total energy with high accuracy and a low computational cost, methods to perform the CI expansion with selected Slater determinants have been investigated [28–31]. The QSCI method uses a quantum computer to select important Slater determinants through the approximate wave function preparation and the subsequent computational-basis measurement. In the HSB-QSCI method, important Slater determinants are sampled from the measurement of the quantum state obtained from the time evolution of an approximate wave function.

A schematic view of the HSB-QSCI method is shown in Figure 1. In the HSB-QSCI, the electronic configurations (Slater determinants) used as the basis for the Hamiltonian matrix are sampled from the time-evolved wave functions $\{|\Phi_k\rangle\}$:

$$|\Phi_k\rangle = e^{-iHk\Delta t} |\Phi_0\rangle. \quad (2)$$

To simulate the real time evolution on a quantum computer, second quantized Hamiltonian given as

$$H = \sum_{pq} h_{pq} a_p^\dagger a_q + \frac{1}{2} \sum_{pqrs} g_{pqrs} a_p^\dagger a_q^\dagger a_s a_r \quad (3)$$

is transformed to a qubit Hamiltonian

$$H_q = \sum_j^J w_j P_j, \quad (4)$$

using a fermion–qubit mapping method. Here, h_{pq} and g_{pqrs} in Eq. (3) are one- and two-electron integrals, respectively, and a_p^\dagger and a_p are the creation and annihilation operators, respectively, acting on the p -th spin orbital. P_j is a tensor product of Pauli operators referred to as a Pauli string, and w_j is its corresponding coefficient computed from h_{pq} and g_{pqrs} . In this work, we used the Jordan–Wigner transformation (JWT) [32] as the fermion–qubit mapping, where each qubit stores the

occupation number of the corresponding spin orbital: $|1\rangle$ if the spin orbital is occupied, and $|0\rangle$ otherwise. In the JWT, the number of qubits required for wave function mapping is equal to the number of spin orbitals in the active space. The quantum circuit for the time evolution operator $U = e^{-iH\Delta t}$ can be constructed using conventional approximate approaches such as the Trotter–Suzuki decomposition [33, 34] and qDRIFT [35], or prepared through classical optimization [9] or via variational quantum algorithms [36].

The initial wave function $|\Phi_0\rangle$ should have an overlap with the target electronic state. The HF wave function $|\psi_{\text{HF}}\rangle$ is a reasonable choice for $|\Phi_0\rangle$ in the electronic ground state calculations of typical closed-shell singlet molecules in their equilibrium geometries, but $|\Phi_0\rangle$ need not be a single Slater determinant. By defining the initial wave function as

$$|\Phi_0\rangle = \sum_l c_l |\Psi_l\rangle, \quad (5)$$

where $|\Psi_l\rangle$ is the l -th eigenfunction of the Hamiltonian, the quantum state after the time evolution is written as follows:

$$|\Phi_k\rangle = \sum_l c_l e^{-iE_l k\Delta t} |\Psi_l\rangle. \quad (6)$$

It is clear that the total evolution time length $k\Delta t$ controls the magnitude of the interferences between the eigenstates, and the measurements of the quantum states in the computational basis with different k can yield different Slater determinants. The information of the sampled Slater determinants is transferred to the classical computer, and the Hamiltonian matrix with the selected configurations is constructed and then diagonalized it to obtain the QSCI wave functions and energies.

The effectiveness of sampling in the HSB-QSCI is mainly controlled by the evolution time length Δt , the number of time steps k , and the initial wave function $|\Phi_0\rangle$. Note that from Eq. (6), we expect that $k\Delta t$ must be set longer for systems with smaller energy gaps with the excited states. In the HSB-QSCI, we can reconstruct $|\Phi_0\rangle$ using the information of the QSCI wave function by constructing a multiconfigurational wave function consisting of several Slater determinants that have large contributions in the QSCI wave function in the previous step. Performing Hamiltonian simulations with different initial wave functions $|\Phi_0\rangle, |\Phi'_0\rangle, |\Phi''_0\rangle, \dots$ and merging the measurement results to perform the QSCI is another option. The availability of such feedback from the subspace Hamiltonian diagonalization part on a classical computer to the state preparation part on a quantum computer is one of the important features of the HSB-QSCI method.

Note that the wave functions are simultaneous eigenfunctions of the Hamiltonian and electron spin \mathbf{S}^2 operator in the non-relativistic regime, but Slater determinants are not always eigenfunctions of the \mathbf{S}^2 operator (spin eigenfunctions). In fact, open-shell Slater determinants with spin- β unpaired electron(s) are not spin eigenfunctions. Here we have assumed that $n_\alpha \geq n_\beta$, where

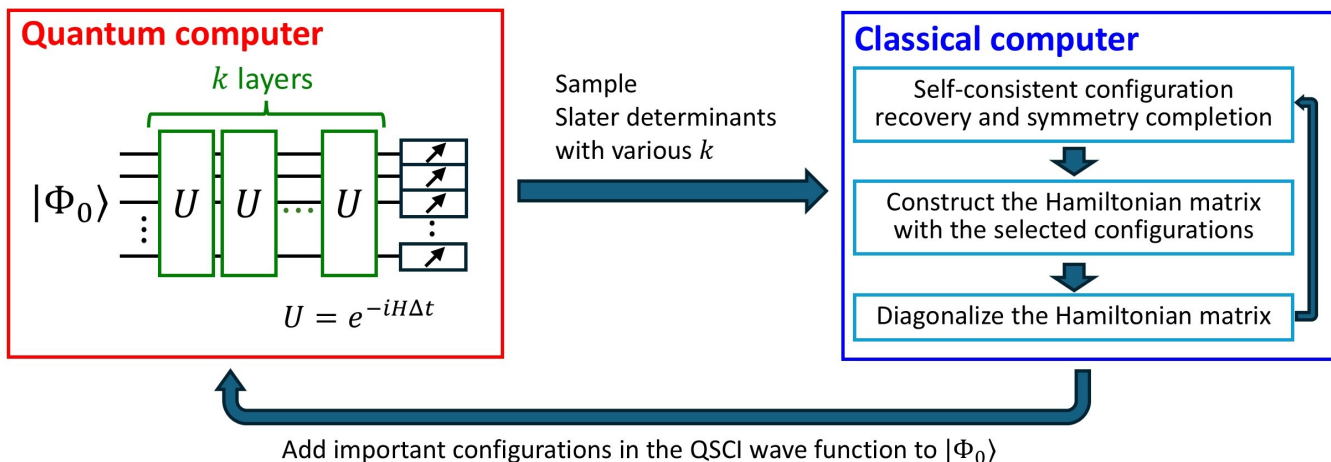


FIG. 1. Schematic view of the HSB-QSCI algorithm.

n_α and n_β are the numbers of spin- α and spin- β electrons, respectively. In order to make the QSCI wave function being spin eigenfunctions, we introduced a symmetry completion step before constructing the subspace Hamiltonian matrix. In the symmetry completion step, open-shell Slater determinants that are missing to span the spin eigenfunction are added. For example, in the spin-singlet state calculations, if the bit string corresponding to the Slater determinant $|2\alpha\alpha\beta\beta 0\rangle$ is sampled (2, α , β , and 0 mean that the corresponding molecular orbital is doubly occupied, singly occupied by a spin- α electron, singly occupied by a spin- β electron, and unoccupied, respectively), then we add $|2\alpha\beta\alpha\beta 0\rangle$, $|2\alpha\beta\beta\alpha 0\rangle$, $|2\beta\beta\alpha\alpha 0\rangle$, $|2\beta\alpha\beta\alpha 0\rangle$, and $|2\beta\alpha\alpha\beta 0\rangle$, if they are not sampled. Similarly for the spin-triplet state, if $|2\alpha\alpha\alpha\beta 0\rangle$ is measured, then we add $|2\alpha\alpha\beta\alpha 0\rangle$, $|2\alpha\beta\alpha\alpha 0\rangle$, and $|2\beta\alpha\alpha\alpha 0\rangle$.

In a case when the Hamiltonian simulations are carried out on a current noisy quantum hardware, the measurements of the quantum state give bit strings that correspond to the Slater determinants with different numbers of electrons. The SCCR proposed recently [19] can be adopted to recover the Slater determinants with a correct number of electrons. In the SCCR, if the bit string obtained from the measurement has the wrong number of electrons, bits are flipped to recover the desired number of electrons, and the probability of bit flipping is determined from the occupation number of the molecular orbital calculated from the QSCI wave function of the previous step. This process is iterated until convergence or the iteration step reaches the predefined maximum steps. The SCCR is performed before symmetry completion.

III. COMPUTATIONAL CONDITIONS

To demonstrate the HSB-QSCI, we performed numerical simulations on a classical computer. The target systems are the S_0 and T_1 states of oligoacenes (**1**, **2**, and **3**), **4** as a representative system of the open-shell singlet

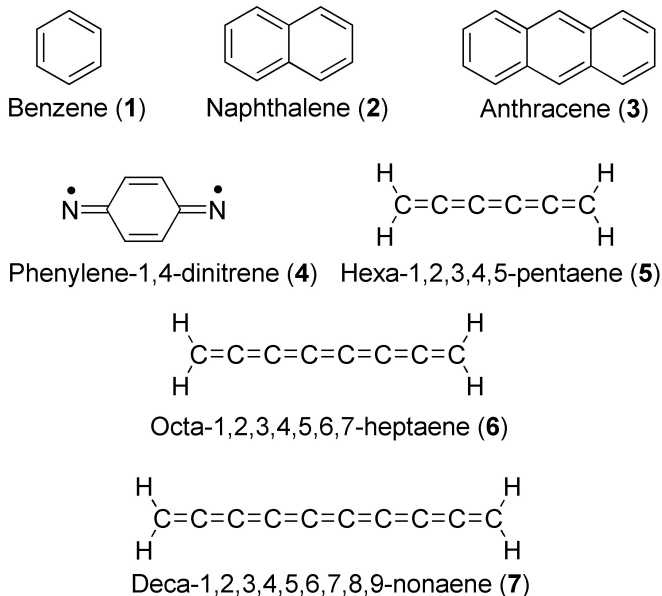


FIG. 2. Target molecules being studied.

ground state, and **5**, as shown in Figure 2. We also performed hardware demonstrations using an IBM Quantum processor for carbyne molecules **5**, **6**, and **7**. Geometry optimizations of oligoacenes and carbynes in planar geometry were performed at the B3LYP/6-31G* level of theory. The twisted geometry of carbynes is generated by rotating one of the CH_2 moieties 90 degrees from the equilibrium geometry. The geometry optimization of **4** was carried out at the CASSCF(10e,10o)/6-31G* level. Here, (N_e, M_o) represents the active space consisting of N electrons and M molecular orbitals. Cartesian coordinates of all molecules are given in Supporting Information.

Since the computational cost of numerical simulations of quantum circuits scales exponentially with the number of qubits, we adopted the active space approxima-

tion. We used the (6e,6o), (10e,10o), and (14e,14o) active spaces for **1**, **2**, and **3**, respectively, which consist of the valence π and π^* orbitals. The one- and two-electron integrals of oligoacenes are calculated at the RHF/STO-3G level. The active space of **4** contains the valence π and π^* orbitals and the in-plane 2p orbital of the nitrogen atoms, and the size is (10e,10o). The CASSCF(10e,10o)/6-31G* molecular orbitals are used to construct the second quantized Hamiltonian of **4**. In the case of carbyne molecules **5**, **6**, and **7** with (10e,10o), (14e,14o), and (18e,18o) active spaces, respectively, the RHF/6-31G* calculation is performed and then the occupied molecular orbitals are localized using the Pipek–Mezey method [37]. For the virtual orbitals, we first formed the singular value decomposition (SVD) quasi-atomic external orbitals using an SVD with respect to the accurate atomic minimal basis functions, and then formed the ordered external orbitals using exchange integrals (using a keyword EXT-LOC=ATMNOS in GAMESS-US software [38]). The active orbitals of all molecules are provided in Figures S1–S10 in Supporting Information. One- and two-electron atomic integrals are obtained from GAMESS-US, and the AO–MO integral transformations were performed using our own Python3 program. The qubit Hamiltonian is then generated using the `OpenFermion` library [39]. All the DFT calculations were done with the Gaussian 16 package [40], and the RHF and CASSCF calculations were carried out with the GAMESS-US software.

As we mentioned in the previous section, the time evolution operation in the HSB-QSCI does not have to be exact, and we can introduce various approximations. In this work, we investigated the effect of Hamiltonian truncation on the sampled Slater determinants in the Hamiltonian simulation and on the QSCI energies. We investigated Hamiltonian truncation based on the locality of the qubit Hamiltonian terms. In this approach, we first generate the localized molecular orbitals (LMOs), and then rearrange the LMOs according to their relative spatial distances. During the qubit Hamiltonian construction using the reordered LMOs, we calculate the locality of the Pauli string (number of Pauli-X, Y, and Z operators in the Pauli string). If the locality of the Pauli string exceeds the threshold, then we exclude it from the qubit Hamiltonian. We investigated this method in **5**, keeping in mind to perform the Hamiltonian simulations on a superconducting quantum device with MPO-based classical compression of the time evolution quantum circuit. The procedure of this step is illustrated in Figure 3.

To sample the Slater determinants based on the real-time evolution of the initial wave function, we set the evolution time for U to be $\Delta t = 1$ and $k = 1, 2, \dots, 10$, unless otherwise noted. To construct the quantum circuit for U , we adopt the first-order Trotter decomposition with a single Trotter slice. Magnitude ordering [41] is used for the Trotterized term ordering. The quantum circuit simulations were done using the `qsim` library [42], which allows us to use GPGPU. The subspace Hamiltonian matrix construction and diagonalization was done using PyCI

library [43], and the SCCR for hardware demonstrations was carried out using `qiskit-addon-sqd` library [44]. It should be noted that the subspace Hamiltonian diagonalization can also be done using `qiskit-addon-sqd`, but it uses a selected CI `kernel.fixed.space` subroutine in PySCF [45] where the spin α and β occupancies are stored separately, and the Slater determinants constructed from all possible combinations of spin α and β strings are used as the basis for the wave function expansion. In this implementation, Slater determinants not sampled by the quantum computer can be included in the subspace Hamiltonian diagonalization, resulting in a quadratic increase in the dimension of the Hamiltonian matrix. This can be seen as a kind of subspace enlargement at the expense of compactness of the QSCI wave function. We also performed a subspace Hamiltonian diagonalization using PySCF, and the results are given in Supporting Information section D. Quantum circuit simulations and the subspace Hamiltonian diagonalization in the QSCI part were performed on the NVIDIA DGX H100 system.

IV. RESULTS AND DISCUSSION

Subsections A, B, C are devoted to show numerical simulations for the S_0 and T_1 states of oligoacenes, phenylene-1,4-dinitrene, and hexa-1,2,3,4,5-pentaene, respectively. Subsection D gives a hardware demonstrations for the S_0 and T_1 states of carbyne molecules.

A. The S_0 and T_1 states of oligoacenes

There is no doubt that aromatic rings are one of the most important molecular skeletons in chemistry, and the study of the electronic structures of oligoacenes is very important. It is known that the zigzag edge of graphene fragments exhibits strong open-shell characters [46], and the contribution of the HF electronic configuration to the full-CI wave function decreases for larger oligoacenes. Electronic excited states of oligoacenes are also of interest because of their potential for various applications such as singlet fission photovoltaics [47].

The results of the HSB-QSCI simulations of oligoacenes are shown in Figure 4. The RHF and ROHF-like single configurational wave functions are used as the starting wave functions for the Hamiltonian simulations of the S_0 and T_1 states, respectively, and the number of shots for each time step was set as 1×10^5 . The number of Slater determinants in the CAS-CI wave function is 104 (S_0) and 61 (T_1) for **1**, 15912 (S_0) and 11076 (T_1) for **2**, and 2945056 (S_0) and 2255121 (T_1) for **3**, in the D_{2h} point group. Our numerical simulations revealed that the Slater determinants that are important to describe the target electronic states are efficiently sampled from the Hamiltonian simulations. In **1**, the system size is very small, and all possible Slater determinants are

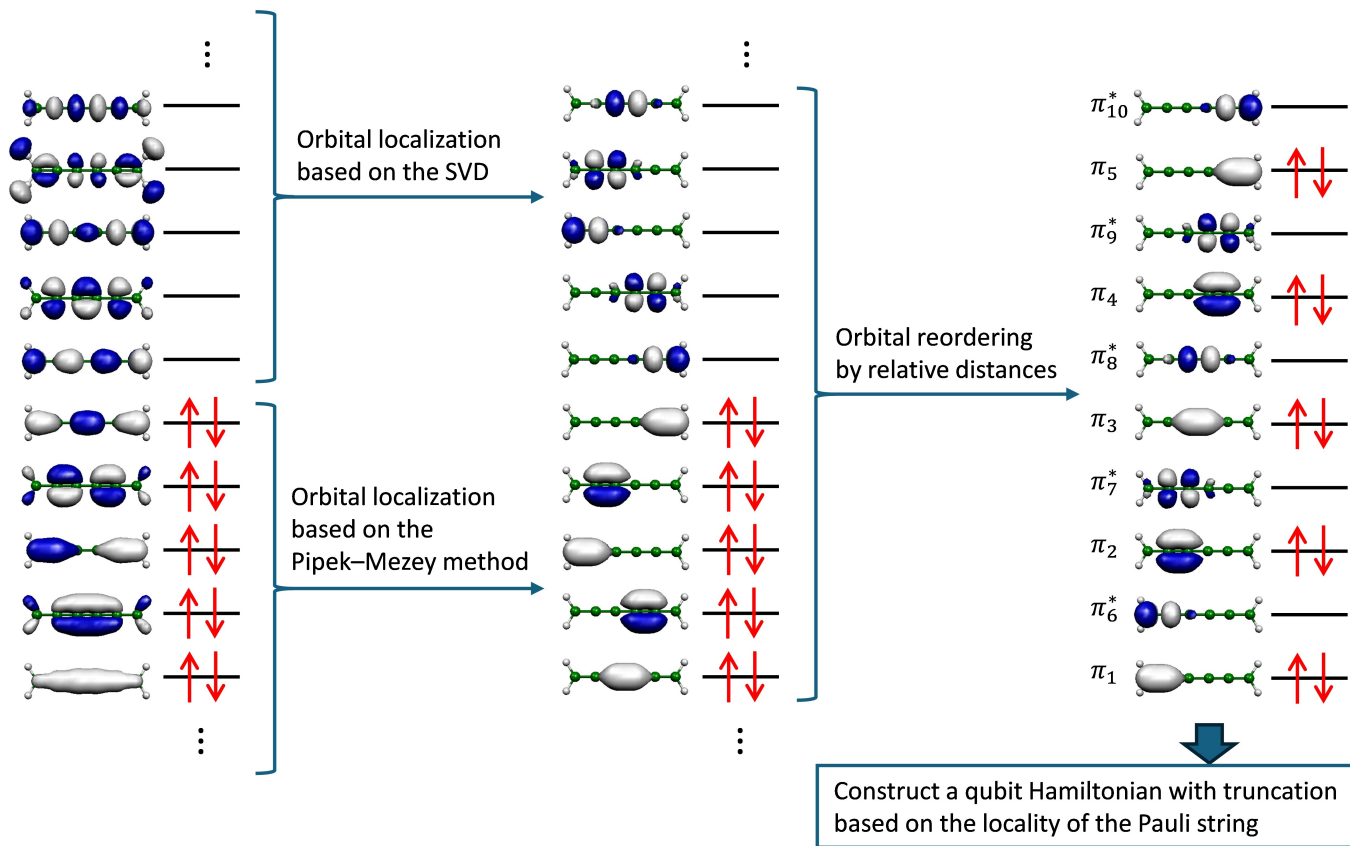


FIG. 3. Procedure of orbital transformations for the Hamiltonian term truncations based on the locality of the Pauli strings, in the case of **5** in its planar geometry. Red arrows indicate the electron occupancies in the RHF wave function.

sampled up to the fifth steps. In **2**, chemical precision ($\Delta E < 1.0 \text{ kcal mol}^{-1}$) was achieved with three steps of the Hamiltonian simulations. In **3**, we found that 10 steps of time evolution with 1×10^5 shots are not enough to achieve chemical precision. We expect that the number of important Slater determinants increases with $\mathcal{O}(M^4)$, which is the same as the scaling of Hamiltonian terms, when the target state wave function is well approximated by the single determinant as in the ground state of oligoacenes and the energy gap between the ground and the first excited states is unchanged. Considering the fact that the energy gap is smaller in **3** than in **2**, we need more than 3.81 times more shots than in the calculation of **2** to obtain the HSB-QSCI energy of **3** with the same accuracy. We have also studied the dependence of the HSB-QSCI energy on the number of shots and the number of time steps in **3**. By increasing the number of shots from 1×10^5 and simulating more time steps, the number of Slater determinants sampled from the Hamiltonian simulation increases, and the HSB-QSCI energy decreases systematically (see Figure S14 in Supporting Information). Although we need more steps and shots to achieve chemical precision for larger systems, it should be noted that up to 7-electron excited determinants were sampled in a Hamiltonian simulation with

$k\Delta t = 1$ in **3**. The ability of Hamiltonian simulations to capture higher-order excitations is astounding. These results illustrate the ability of the Hamiltonian simulation to sample a polynomial number of important Slater determinants from exponentially large Hilbert space. When the `kernel_fixed_space` subroutine in PySCF is used for subspace Hamiltonian diagonalization, chemical precision was achieved with only three steps of time evolutions with 1×10^5 shots in **3**. However, the HSB-QSCI wave function considers about 57% and 46% of the Slater determinants, hence the HSB-QSCI wave function is less compact (see Figure S11 in Supporting Information).

B. The S_0 and T_1 states of phenylene-1,4-dinitrene

4 has two major resonance structures, the diradical with a quinonoid skeleton as shown in Figure 2, and the dinitrene with an aromatic ring. Its electronic ground state is an open-shell spin-singlet state with two unpaired electrons in in-plane 2p orbitals of the nitrogen atoms. The thermally excited spin-triplet state of **4** has been observed by ESR spectroscopy [48–50], and the singlet-triplet energy gap is determined to be $0.82 \text{ kcal mol}^{-1}$ from the Curie analysis of the ESR signal [51]. The ex-

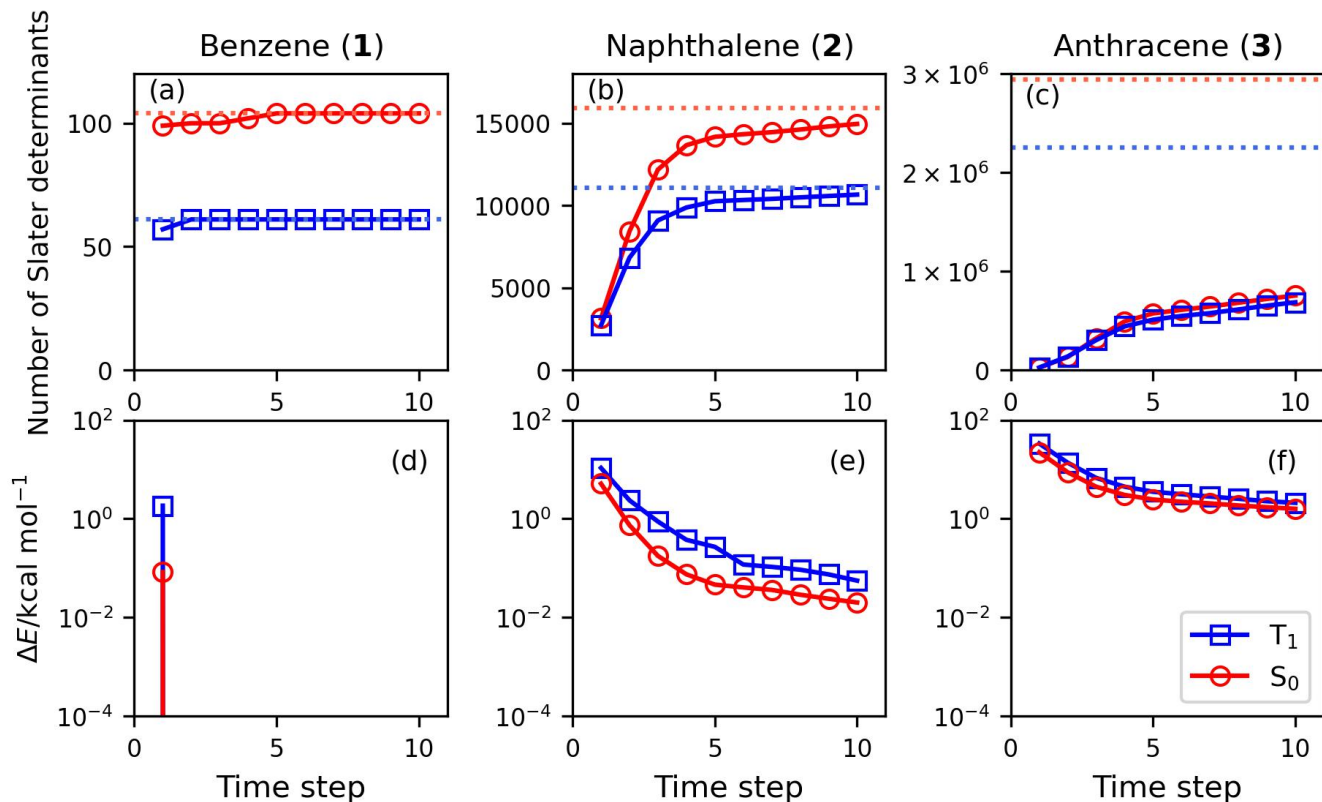


FIG. 4. HSB-QSCI results of oligoacenes. The number of Slater determinants included in the Hamiltonian diagonalization is given in (a), (b), and (c) for **1**, **2**, and **3**, respectively. Red and blue indicate the S_0 and T_1 states, respectively. Dotted lines represent the number of Slater determinants in the CAS-CI wave function. The difference of the HSB-QSCI energy from the CAS-CI values in units of kcal mol^{-1} are given in (d), (e), and (f) on the logarithmic scale.

perimentally determined zero-field splitting parameter in the excited spin-triplet state is $|D| = 0.171 \text{ cm}^{-1}$ [48], which is about 10 times larger than the value estimated from a point-dipole approximation. This deviation was explained by the lack of electron correlation effect in the point-dipole approximation [52], insisting that sophisticated consideration of electronic correlation is essential to describe its electronic structure.

In the CASSCF optimized orbital basis, the CAS-CI wave function of the S_0 state is mainly described by the HF configuration ($|\psi_{\text{HF}}\rangle$) and the HOMO–LUMO two-electron excited configuration from the HF configuration ($|\psi_{2e}\rangle$) (see Table S17 in Supporting Information). In the HSB-QSCI simulations of the S_0 state, we performed Hamiltonian simulations with three different initial wave functions, $|\psi_{\text{HF}}\rangle$, $|\psi_{2e}\rangle$, and the CAS-CI(2e,2o) wave function $|\Psi_{\text{CAS22}}\rangle = 0.7138 |\psi_{\text{HF}}\rangle - 0.7003 |\psi_{2e}\rangle$, to investigate the dependence of the initial wave function on the energies and the convergence behavior of the HSB-QSCI method. The QSCI simulations were performed under four different conditions: (1) use the $|\psi_{\text{HF}}\rangle$ results with 1×10^5 shots for each time step, (2) use the $|\psi_{2e}\rangle$ with 1×10^5 shots, (3) use the samples from $|\Psi_{\text{CAS22}}\rangle$ with 1×10^5 shots, and (4) merge the samples from $|\psi_{\text{HF}}\rangle$ and $|\psi_{2e}\rangle$ with 5×10^4 shots for each step. For the T_1 state, we

used the ROHF-like single determinant as the initial wave function for the Hamiltonian simulation. The HSB-QSCI results are summarized in Figure 5. Our numerical simulations suggest that almost the same number of Slater determinants are sampled when $|\psi_{\text{HF}}\rangle$ and $|\psi_{2e}\rangle$ are used. Interestingly, the number of Slater determinants sampled from the Hamiltonian simulation is smaller when $|\Psi_{\text{CAS22}}\rangle$ is used as the initial wave function. The accuracy of the HSB-QSCI energy with $|\Psi_{\text{CAS22}}\rangle$ is about an order of magnitude worse than the HF-reference one, but still chemical precision was achieved in 2 steps of time evolution. The singlet–triplet energy gap is calculated to be $1.11 \text{ kcal mol}^{-1}$, in good agreement with the CAS-CI value ($1.06 \text{ kcal mol}^{-1}$) and the experimental one [51]. Using PySCF for the subspace Hamiltonian diagonalization slightly increases the number of Slater determinants and yields lower HSB-QSCI energies. The trends of the initial wave function dependence are similar between PyCI- and PySCF-based implementations (see Figure S12 in the Supporting Information).

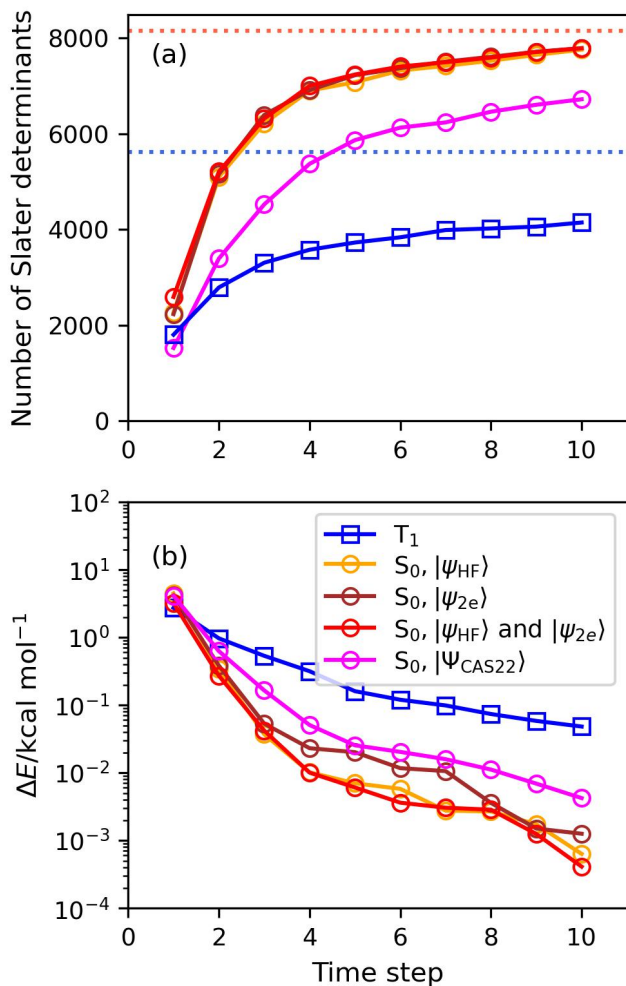


FIG. 5. HSB-QSCI results of 4. (a) The number of Slater determinants sampled from Hamiltonian simulations. The red and blue dotted lines indicate the number of Slater determinants in the CAS-CI wave function. (b) The difference of the HSB-QSCI energy from the CAS-CI values in units of kcal mol⁻¹, on the logarithmic scale.

C. The S₀ and T₁ states of hexa-1,2,3,4,5-pentaene

Our last example of numerical simulations is the S₀ and T₁ states of **5**. From the DFT calculations, the carbyne with =CH₂ termination is predicted to have a helical π conjugation in the non-planar geometries [53, 54]. In the S₀ state, the planar structure is the energy minimum, but in the T₁ state, the planar geometry is a saddle point and the twisted geometry becomes stable. As a result, the singlet-triplet energy gap strongly depends on the dihedral angle between two =CH₂ terminations. In this study, we calculated the S₀ and T₁ states of the geometries with the dihedral angles of 0° and 90°.

Because carbyne is a one-dimensional molecule, using LMOs and adopting Hamiltonian truncation by maximum locality may be a good option to reduce the com-

putational cost of Hamiltonian simulation. In this work, we investigated Hamiltonian term truncation by operator locality of the Pauli string in the qubit Hamiltonian. By reordering the LMOs by relative distances before constructing a qubit Hamiltonian, operator locality-based truncation is roughly equivalent to Hamiltonian term truncation based on spatial distances. To assess the effect of Hamiltonian truncation with the locality, we first calculated the number of Hamiltonian terms in the second quantized Hamiltonian and the fidelity of the ground state wave function, $|\langle \Psi_0(\text{truncated}) | \Psi_0(\text{full}) \rangle|^2$, where $|\Psi_0(\text{truncated})\rangle$ and $|\Psi_0(\text{full})\rangle$ are the ground state wave functions with the truncated and untruncated Hamiltonians, respectively. The results are summarized in Tables I and II for planar and twisted geometries, respectively.

TABLE I. Number of terms in the second quantized Hamiltonian and fidelity of the electronic ground state wave function of **5** in planar geometry.

Maximum locality m	#Terms	Fidelity
20	20072	1.0
18	19676	0.999816
16	18596	0.998764
14	17592	0.998571
12	16248	0.996394
10	12708	0.992327
8	7836	0.946569
6	4840	0.941506
4	3048	0.912734

TABLE II. Number of terms in the second quantized Hamiltonian and fidelity of the electronic ground state wave function of **5** in twisted geometry.

Maximum locality m	#Terms	Fidelity
20	40200	1.0
18	39772	0.999576
16	38244	0.997395
14	35232	0.996860
12	30640	0.995021
10	24660	0.987597
8	17772	0.898829
6	10744	0.891525
4	4632	0.843284

Note that the number of Hamiltonian terms is larger in the twisted geometry than in the planar one, which is due to the difference in the spatial distribution of π orbitals. In planar geometry, the one-electron MO integrals between the nearest neighbor π orbitals (e.g., π_1 and π_2 in Figure 3) are zero, while in twisted geometry, they are non-zero due to helical π conjugations. As can be seen from Tables I and II, the number of Hamiltonian terms is reduced by about 40% when considering up to 10-local terms, with the fidelity of the ground state wave function being about 0.99. The rapid decrease of the fidelity for the maximum locality smaller than 10 can be explained by the fact that the π_x - π_x and π_y - π_y interactions (here we assumed that one-dimensional carbon

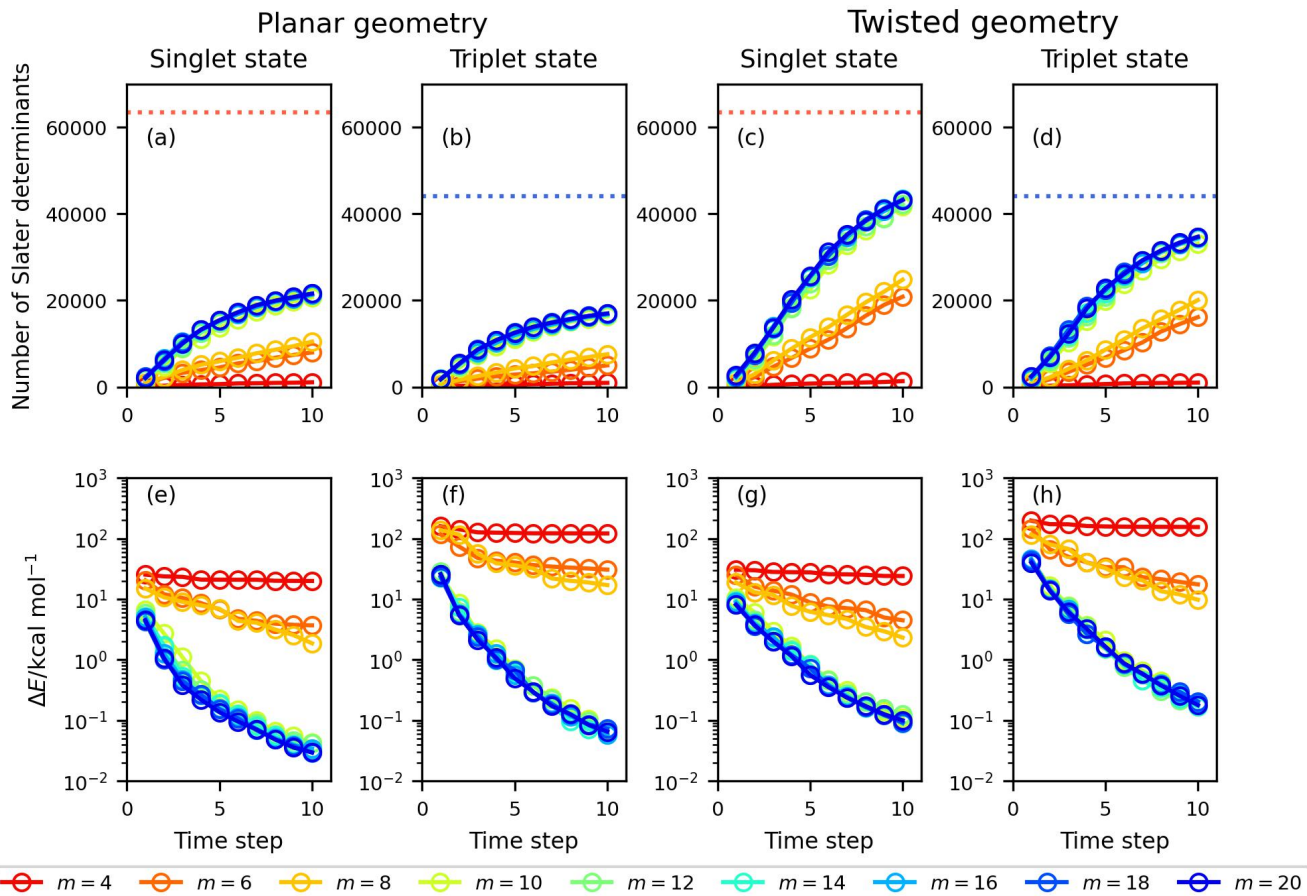


FIG. 6. HSB-QSCI results of **5** in its planar and twisted geometries with different maximum locality values m . The number of Slater determinants included in the Hamiltonian diagonalization is given in (a), (b), (c), and (d). The red and blue dotted lines represent the number of Slater determinants in the CAS-CI wave function of the S_0 and T_1 states, respectively. The difference of the HSB-QSCI energy from the CAS-CI values in units of kcal mol^{-1} are given in (e), (f), (g), and (h) on the logarithmic scale.

atom chain is parallel to the z -axis) with the next nearest neighbor C=C bond (for example, π_1 – π_3 in Figure 3) are described as 10-local operators in the qubit Hamiltonian.

The results of the HSB-QSCI simulations are shown in Figure 6. The number of shots for each time step is 1×10^5 . In the T_1 state calculations, we set the starting wave function to carry two unpaired electrons in the central π bonds (π_3 and π_8^* in Figure 3). It is clear that the number of Slater determinants sampled from the Hamiltonian simulations and the convergence behavior of the HSB-QSCI energies are almost the same for $m \geq 10$, where m is the maximum locality of the qubit Hamiltonian terms. These results are consistent with the trend of the S_0 state fidelity value. The singlet–triplet energy gap $\Delta E_{S-T} = E_S - E_T$ calculated using the real-time evolution with the untruncated Hamiltonian ($m = 20$) is -53.96 and $-20.33 \text{ kcal mol}^{-1}$ for planar and twisted geometries, respectively, and the difference from the CAS-CI singlet–triplet energy gap is less than $0.1 \text{ kcal mol}^{-1}$ ($\Delta E_{S-T}(\text{CAS-CI}) = -53.93$ and $-20.26 \text{ kcal mol}^{-1}$ for

planar and twisted geometry, respectively). The number of sampled Slater determinants is larger for twisted geometry than for planar geometry, reflecting the spatial distribution of the π orbitals, as discussed above. When the maximum locality is set to be $m = 6$ or 8 , the error in the HSB-QSCI energy becomes larger. However, our numerical simulations revealed that chemical precision can be achieved even with the maximum locality $m = 6$, by increasing the number of shots to more than 3×10^6 and setting the number of maximum time steps to $k = 20$ (see Figure S15 in Supporting Information). Note that when using the PySCF `kernel_fixed_space` subroutine for subspace Hamiltonian diagonalization, chemical precision was achieved with up to five steps of time evolution with 10^5 shots (see Figure S14 in Supporting Information), but this is a consequence of the quadratic increase of the Slater determinants in PySCF.

It should be emphasized that the ROHF-like single configurational wave function in the LMO basis used in the T_1 state calculation has rather a small overlap with

the CAS-CI wave function. The squared overlap values $|\langle \Phi_0 | \Psi_{\text{CAS-CI}} \rangle|^2$ in the T_1 state are 0.1691 and 0.1240 for planar and twisted geometries, respectively (see Tables S16 and S18 in Supporting Information for the CAS-CI wave function). The fact that the HSB-QSCI provides accurate energy with such a small overlap is promising because the overlap between the HF and the full-CI wave functions decreases with system size, and the preparation of a sophisticated approximate wave function becomes challenging for larger molecules.

D. Hardware demonstration of the HSB-QSCI calculations of the S_0 and T_1 states of carbyne molecules

Since the Hamiltonian term truncation based on the locality of the qubit Hamiltonian terms works excellently in **5**, we performed the HSB-QSCI calculations of **5**, **6**, and **7** on an IBM Quantum Eagle processor, namely `ibm_kawasaki`. To reduce the quantum circuit depth of the Hamiltonian simulation, we performed the MPO-based classical compression of the quantum circuit. This approach was demonstrated in our previous study on the quantum phase difference estimation-based energy gap calculations [9]. The details of the MPO-based quantum circuit optimization are given in the reference [9]. In this work, we used a Hamiltonian truncated by the maximum locality ($m = 10$), and the 10-layer brick wall type quantum circuit is generated for the time evolution operator of $\Delta t = 1$. The number of sweeps on the optimizations was set to 10000. In constructing the MPOs, the second-order Trotter decomposition with a single Trotter slice was employed, and the singular value cutoff for the SVD was set to 10^{-4} . The order of terms in the Trotter decomposition is set as follows. First, we generate the truncated second quantized Hamiltonian by checking the one- and two-electron integrals in the lexicographic order: q after p in h_{pq} , and p, r, q, s , in that order in g_{pqrs} . Then the truncated second-quantized Hamiltonian is transformed into a qubit Hamiltonian while retaining the order of the terms, and the Trotterized time evolution operator is constructed subsequently.

We first checked the Hamming weight distribution of the bit strings obtained in the measurements and compared it to the uniform distribution. The Hamming weight distributions at $k\Delta t = 10$ are plotted in Figure 7. We confirmed that the Hamming weight distributions of the bit strings obtained from the Hamiltonian simulation with $k\Delta t = 10$ are significantly different from the uniform distribution. However, due to hardware noise, only 11–23% of the measured bit strings have correct Hamming weights (10, 14, and 18 for **5**, **6**, and **7**, respectively).

The HSB-QSCI results of **5** are summarized in Figure 8. Here, the Hamiltonian simulations were carried out with $k = 10$, and the number of shots was set from 1×10^5 to 1×10^6 . The depth of the quantum circuit after transpilation with optimization level = 3 in qiskit is 21, re-

gardless of the evolution time steps. The SCCR [19] was adopted to recover configurations with a correct number of electrons, before constructing the subspace Hamiltonian matrix. In the first five to eight steps of time evolution, the number of Slater determinants sampled increases rapidly, but thereafter the number of additionally sampled Slater determinants becomes gradual. When the HSB-QSCI is performed up to ten steps of time evolution and 1×10^5 shots for each time step, the energy error is about 2 kcal mol $^{-1}$. Increasing the number of shots further improves the energy, and the error in the total energy with 1×10^6 shots were 0.37, 0.56, 0.33, and 0.43 kcal mol $^{-1}$ for planar (S_0), planar (T_1), twisted (S_0), and twisted (T_1), respectively, achieving chemical precision.

The dimensions of the Hamiltonian matrix and the total energies of the HSB-QSCI and the CAS-CI methods are summarized in Table III. We used $k = 10$ and performed 3×10^6 shots for each time step in the HSB-QSCI for **6** and **7**. In **6**, the HSB-QSCI considered about 50–64% of the entire Slater determinant, and it calculated the total energy with an error of about 2.0–2.9 kcal mol $^{-1}$. Although chemical precision for the total energy was not achieved, the HSB-QSCI provides the singlet–triplet energy gap with an error of 0.93 and 0.12 kcal mol $^{-1}$ for planar and twisted geometries, respectively, of **6**. The energy difference between the planar and twisted geometries is also calculated with an error of about 0.72 and 0.09 kcal mol $^{-1}$ for the S_0 and T_1 states, respectively. These results exemplify the ability of the HSB-QSCI to accurately calculate energy differences between two electronic states and two geometries. We expect that the total energy can be further improved by increasing the number of shots in the Hamiltonian simulation. In **7**, the error of the HSB-QSCI energy is about 14 kcal mol $^{-1}$ for the S_0 state, and it increases to 23.36 and 25.79 kcal mol $^{-1}$ for planar and twisted geometries, respectively, of the T_1 state. Again, chemical precision for the total energy was not achieved in **7**. In addition, the HSB-QSCI overestimated the singlet–triplet energy gap about 9–12 kcal mol $^{-1}$. As we pointed out above, the CAS-CI wave function of the T_1 state in the localized orbital basis shows an inherent multiconfigurational character, and the single Slater determinant used as the initial wave function of the time evolution has small overlap with the CAS-CI wave function. As a result, it is expected that the number of time steps or the number of shots will have to be increased to account for more Slater determinants in order to accurately describe the electronic structure of the T_1 state. Nevertheless, it is worth noting that the HSB-QSCI is able to compute the energy difference between the planar and twisted geometries of the S_0 state with chemical precision. Note that when PySCF is used for the subspace Hamiltonian diagonalization, the HSB-QSCI provided the total energy of the S_0 state with about 0.3 kcal mol $^{-1}$ of an error, by considering 46–48% of the Slater determinants, but it failed to compute the total energy of the T_1 state with chemical precision.

Table IV summarizes the percentages of the number of

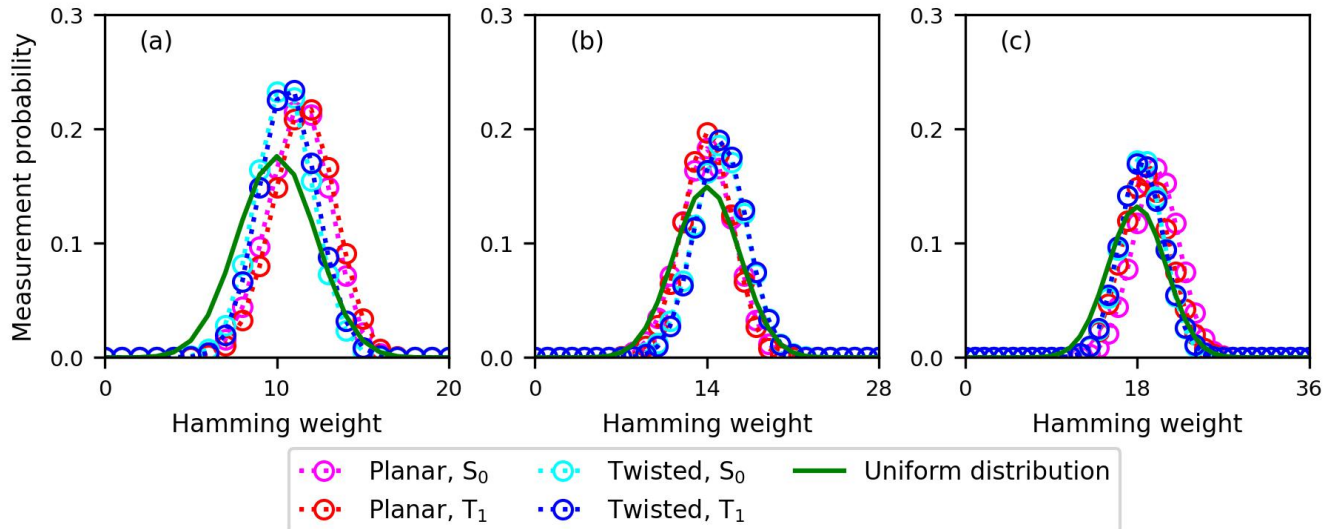


FIG. 7. Hamming weight distribution of the bit strings obtained from measurements after Hamiltonian simulation of carbyne molecules with $k\Delta t = 10$, using `ibm_kawasaki`. (a) **5**, (b) **6**, and (c) **7**

TABLE III. Number of Slater determinants and total energies of the CAS-CI and the number of selected Slater determinants and the error of the HSB-QSCI energy calculated using `ibm_kawasaki`.

System	CAS-CI		HSB-QSCI; PyCI		HSB-QSCI; PySCF	
	#Dets	$E/\text{Hartree}$	#Dets	$\Delta E/\text{kcal mol}^{-1}$	#Dets	$\Delta E/\text{kcal mol}^{-1}$
5 (Planar, S_0)	63504	-229.5024030030	52209	0.37	63504	0.00
5 (Planar, T_1)	44100	-229.4164659619	40092	0.56	44100	0.00
5 (Twisted, S_0)	63504	-229.4452184415	54585	0.33	63504	0.00
5 (Twisted, T_1)	44100	-229.4129399110	40944	0.43	43260	0.01
6 (Planar, S_0)	11778624	-305.2359857689	6147941	2.00	11778624	0.00
6 (Planar, T_1)	9018009	-305.1666727092	5753210	2.93	8612604	0.01
6 (Twisted, S_0)	11778624	-305.1941677868	5838894	2.71	11758041	0.00
6 (Twisted, T_1)	9018009	-305.1698864405	5440991	2.84	8889232	0.00
7 (Planar, S_0)	2363904400	-380.9720622554	22569820	14.26	1141628944	0.31
7 (Planar, T_1)	1914762564	-380.9133659533	14732855	23.36	526263465	3.70
7 (Twisted, S_0)	2363904400	-380.9394312061	25866058	13.97	1096536996	0.30
7 (Twisted, T_1)	1914762564	-380.9186151034	16356089	25.79	554484410	2.40

Slater determinants and the correlation energies covered by the HSB-QSCI method in **5–7**. It is worth emphasizing that the HSB-QSCI covers more than 99.75% of the correlation energies in the active space in **7**, by considering only ca. 1% of all the Slater determinants.

V. CONCLUSION

In this study, we proposed an HSB-QSCI, which uses a quantum computer to perform Hamiltonian simulation and subsequent measurement of the quantum state in the computational basis to sample the important Slater determinants used to span the subspace Hamiltonian to be diagonalized on a classical computer. Compared to the reported VQE-based state preparation approaches for the QSCI [14, 16, 17], the HSB-QSCI is free from variational optimizations of the quantum states, and it works

with the simple initial wave function like the HF. Since long-time evolution is in general difficult to simulate on a classical computer, we expect this approach to become powerful as the system size increases. Proof-of-concept simulations were performed for the S_0 and T_1 states of organic molecules **1–5**, and we achieved chemical precision in all molecules studied. The quantum hardware demonstrations of the HSB-QSCI for the S_0 and T_1 states of three carbyne molecules **5–7** were also reported using `ibm_kawasaki` with 20, 28, and 36 qubits, respectively, with the aid of MPO-based classical optimization of the quantum circuit for the time evolution operator. The HSB-QSCI achieved chemical precision for the total energy in **5**, for the singlet–triplet energy difference in **6**, and for the energy difference between planar and twisted geometries of the S_0 state in **7**. In **7**, by considering about 1% of the Slater determinants, the HSB-QSCI captured more than 99.75% of correlation energies in the active

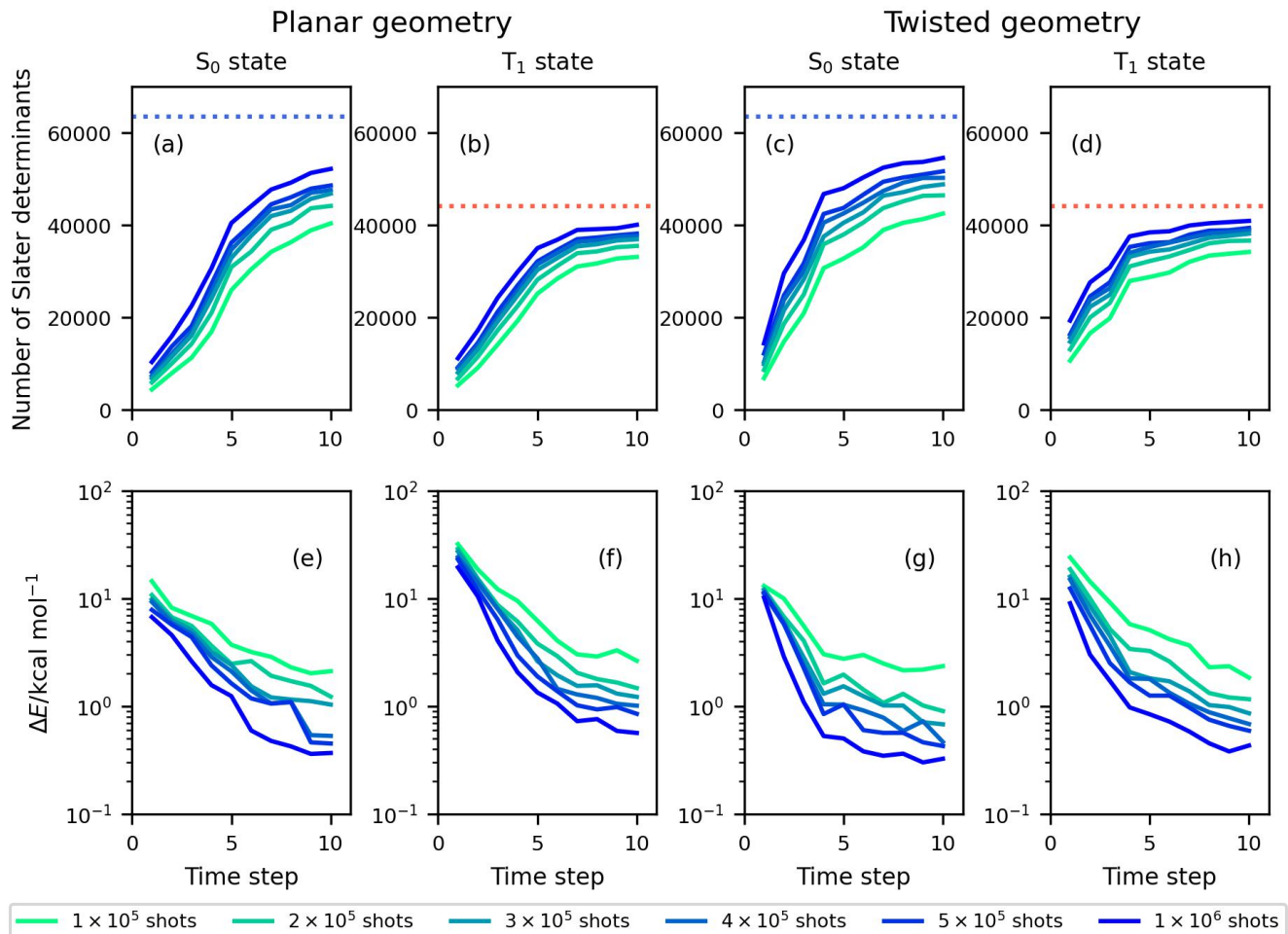


FIG. 8. HSB-QSCI results of **5** obtained with a Hamiltonian truncated by the maximum locality $m = 10$ and `ibm_kawasaki`, with SCCR. The number of Slater determinants included in the Hamiltonian diagonalization are given in (a), (b), (c), and (d), and the difference of the HSB-QSCI energy from the CAS-CI values in units of kcal mol^{-1} are given in (e), (f), (g), and (h) on the logarithmic scale.

space. The largest system studied in this work is **7** with 36 qubits, which is the largest system capable of performing the CAS-CI calculation in a typical computational environment without a supercomputer [45, 55]. We expect that the HSB-QSCI can handle the system larger than 36 qubits, by introducing batch-based implementations in the Hamiltonian matrix diagonalization part, and calculating the variance of the energy expectation value $\Delta H = \langle \Psi | H^2 | \Psi \rangle - \langle \Psi | H | \Psi \rangle^2$ as explored in Reference [19]. Note that, as discussed by Reinholdt and coworkers in their recent paper [56], the QSCI wave function is in some cases less compact than that obtained by classical heuristics. From Eq. (6), the probability that a particular Slater determinant is measured in the HSB-QSCI depends not only on the CI coefficient of the ground state, but also on the gap to the excited state and the CI coefficient of the excited state, and screening out unimportant Slater determinants from the subspace is very important in the application to larger systems. Apply-

ing the auxiliary-field quantum Monte Carlo (AFQMC) method with the QSCI wave function as the input can be another direction towards larger-scale quantum chemical calculations with a quantum computer, as suggested in recent studies [57, 58]. Application of the HSB-QSCI to larger systems is currently in progress.

VI. ACKNOWLEDGMENTS

This work was supported by Quantum-LEAP Flagship Program (Grant No. JPMXS0120319794 and JPMXS0118067285) from Ministry of Education, Culture, Sports, Science and Technology (MEXT), Japan. K.S. acknowledges support from Center of Innovations for Sustainable Quantum AI (JPMJPF2221) from Japan Science and Technology Agency (JST), Japan and Grants-in-Aid for Scientific Research C (21K03407) and for Transformative Research Area B (23H03819) from Japan

TABLE IV. Percentages of the number of Slater determinants and the correlation energies in the active space covered by the HSB-QSCI.

System	%#Dets ^a	%E _{Corr} ^b
5 (Planar, S ₀)	82.21	99.99
5 (Planar, T ₁)	90.91	99.98
5 (Twisted, S ₀)	85.96	99.99
5 (Twisted, T ₁)	92.84	99.99
6 (Planar, S ₀)	52.20	99.97
6 (Planar, T ₁)	63.80	99.96
6 (Twisted, S ₀)	49.57	99.96
6 (Twisted, T ₁)	60.33	99.96
7 (Planar, S ₀)	0.95	99.86
7 (Planar, T ₁)	0.77	99.78
7 (Twisted, S ₀)	1.09	99.87
7 (Twisted, T ₁)	0.87	99.75

^a Percentage of the number of Slater determinants calculated as $100 \times \frac{\#Dets(\text{HSB-QSCI})}{\#Dets(\text{CAS-CI})}$.

^b Percentage of the correlation energy in the active space considered in the HSB-QSCI, calculated as $100 \times \frac{E(\text{Ref}) - E(\text{HSB-QSCI})}{E(\text{Ref}) - E(\text{CAS-CI})}$.

Society for the Promotion of Science (JSPS), Japan. A part of this work was performed for Council for Science, Technology and Innovation (CSTI), Cross-ministerial Strategic Innovation Promotion Program (SIP), “Promoting the application of advanced quantum technology platforms to social issues” (Funding agency: QST). The authors thank Takashi Abe, Yoshiharu Mori, and Hajime Nakamura for useful discussions. The part of calculations was performed on the Mitsubishi Chemical Corporation (MCC) high-performance computer (HPC) system “NAYUTA”, where “NAYUTA” is a nickname for MCC HPC and is not a product or service name of MCC. We acknowledge the use of IBM Quantum services for this work. The views expressed are those of the authors, and do not reflect the official policy or position of IBM or the IBM Quantum team.

- [1] A. Aspuru-Guzik, A. D. Dutoi, P. J. Love, and M. Head-Gordon. Simulated quantum computation of molecular energies. *Science*, 309:1704–1707, 2005.
- [2] B. P. Lanyon, J. D. Whitfield, G. G. Gillett, M. E. Goggin, M. P. Almeida, I. Kassal, J. D. Biamonte, M. Mohseni, B. J. Powell, M. Barbieri, A. Aspuru-Guzik, and A. G. White. Towards quantum chemistry on a quantum computer. *Nat. Chem.*, 2:106–111, 2010.
- [3] J. Du, N. Xu, X. Peng, P. Wang, S. Wu, and D. Lu. NMR implementation of a molecular hydrogen quantum simulation with adiabatic state preparation. *Phys. Rev. Lett.*, 104:030502, 2010.
- [4] Y. Wang, F. Dolde, J. Biamonte, R. Babbush, V. Bergholm, S. Yang, I. Jakobi, P. Neumann, A. Aspuru-Guzik, J. D. Whitfield, and J. Wrachtrup. Quantum simulation of helium hydride cation in a solid-state spin register. *ACS Nano*, 9:7769–7774, 2015.
- [5] P. J. J. O’Malley, R. Babbush, I. D. Kivlichan, J. Romero, J. R. McClean, R. Barends, J. Kelly, P. Roushan, A. Tranter, N. Ding, B. Campbell, Y. Chen, Z. Chen adn B. Chiaro, A. Dunsworth, A. G. Fowler, E. Jeffrey, E. Lucero, A. Megrant, J. Y. Mutus, M. Neeley, C. Neill, C. Quintana, D. Sank, A. Vainsencher, J. Wenner, T. C. White, P. V. Coveney, P. J. Love, H. Neven, A. Aspuru-Guzik, and J. M. Martinis. Scalable quantum simulation of molecular energies. *Phys. Rev. X*, 6:031007, 2016.
- [6] R. Santagati, J. Wang, A. A. Gentile, S. Paesani, N. Wiebe, J. R. McClean, S. Morley-Short, P. J. Shatbolot, D. Bonneau, J. W. Silverstone, D. P. Tew, X. Zhou, J. L. O’Brien, and M. G. Thompson. Witnessing eigenstates for quantum simulation of Hamiltonian spectra. *Sci. Adv.*, 4:eaap9646, 2018.
- [7] N. S. Blunt, L. Caune, R. Izsak, E. T. Campbell, and N. Holzmann. Statistical phase estimation and error mitigation on a superconducting quantum processor. *PRX Quantum*, 4:040341, 2023.
- [8] K. Yamamoto, S. Duffield, Y. Kikuchi, and D. Muñoz Ramo. Demonstrating Bayesian quantum phase estimation with quantum error detection. *Phys. Rev. Res.*, 6:013221, 2024.
- [9] S. Kanno, K. Sugisaki, H. Nakamura, H. Yamauchi, R. Sakuma, T. Kobayashi, Q. Gao, and N. Yamamoto. Tensor-based quantum phase difference estimation for large-scale demonstration. arXiv:2408.04946, 2024.
- [10] A. Peruzzo, J. McClean, P. Shadbolt, M.-H. Yung, X.-Q. Zhou, P. J. Love, A. Aspuru-Guzik, and J. L. O’Brien. A variational eigenvalue solver on a photonic quantum processor. *Nat. Comm.*, 5:4213, 2014.
- [11] J. Tilly, H. Chen, S. Cao, D. Picozzi, K. Setia, Y. Li, E. Grant, L. Wossnig, I. Rungger, G. H. Booth, and J. Tennyson. The variational quantum eigensolver: a review of methods and best practices. *Phys. Rep.*, 986:1–128, 2022.
- [12] J. F. Gonthier, M. D. Radin, C. Buda, E. J. Doskocil, C. M. Abuan, and J. Romero. Measurements as a roadblock to near-term physical quantum advantage in chemistry: Resource analysis. *Phys. Rev. Res.*, 4:033154, 2022.
- [13] J. R. McClean, S. Boixo, V. N. Smelyanskiy, R. Babbush, and H. Neven. Barren plateaus in quantum neural network training landscapes. *Nat. Comm.*, 9:4812, 2018.
- [14] K. Kanno, M. Kohda, R. Imai, S. Koh, K. Mitarai, W. Mizukami, and Y. O. Nakagawa. Quantum-selected configuration interaction: classical diagonalization of Hamiltonians in subspaces selected by quantum computers. arXiv:2302.11320, 2023.
- [15] H. R. Grimsley, S. E. Economou, E. Barnes, and N. J. Mayhall. An adaptive variational algorithm for exact molecular simulations on a quantum computer. *Nat. Comm.*, 10:3007, 2019.
- [16] Y. O. Nakagawa, M. Kamoshita, W. Mizukami, S. Sudo, and Y. Ohnishi. ADAPT-QSCI: adaptive construction of input state for quantum-selected configuration interaction. *J. Chem. Theory Comput.*, 20:10817–10825, 2024.

- [17] L. Nützel, A. Gresch, L. Hehn, L. Marti, R. Freund, A. Steiner, C. D. Marciniak, T. Eckstein, N. Stockinger, S. Wolf, T. Monz, M. Kühn, and M. J. Hartmann. Solving an industrially relevant quantum chemistry problem on quantum hardware. *Quantum Sci. Technol.*, 10:015066, 2025.
- [18] M. Motta, K. J. Sung, K. Birgitta Whaley, M. Head-Gordon, and J. Shee. Bridging physical intuition and hardware efficiency for correlated electronic states: the local unitary cluster Jastrow ansatz for electronic structure. *Chem. Sci.*, 14:11213–11227, 2023.
- [19] J. Robledo-Moreno, M. Motta, H. Haas, A. Javadi-Abhari, P. Jurcevic, W. Kirby, S. Martiel, K. Sharma, S. Sharma, T. Shirakawa, I. Sitdikov, R.-Y. Sun, K. J. Sung, M. Takita, M. C. Tran, S. Yunoki, and A. Mezzacapo. Chemistry beyond exact solutions on a quantum-centric supercomputer. arXiv:2405.05068, 2024.
- [20] D. Kaliakin, A. Shajan, J. Robledo Moreno, Z. Li, A. Mitra, M. Motta, C. Johnson, A. Ash Saki, S. Das, I. Sitdikov, A. Mezzacapo, and K. M. Merz Jr. Accurate quantum-centric simulations of supramolecular interactions. arXiv:2410.09209, 2024.
- [21] S. Barison, J. Robledo Moreno, and M. Motta. Quantum-centric computation of molecular excited states with extended sample-based quantum diagonalization. *Quantum Sci. Technol.*, 10:025034, 2025.
- [22] I. Liepuoniute, K. D. Doney, J. Robledo Moreno, J. A. Job, W. S. Friend, and G. O. Jones. Quantum-centric study of methylene singlet and triplet states. arXiv:2411.04827, 2024.
- [23] A. Shajan, D. Kaliakin, A. Mitra, J. Robledo Moreno, Z. Li, M. Motta, C. Johnson and A. Ash Saki, S. Das, I. Sitdikov, A. Mezzacapo, and K. M. Merz Jr. Towards quantum-centric simulations of extended molecules: sample-based quantum diagonalization enhanced with density matrix embedding theory. arXiv:2411.09861, 2024.
- [24] After posting this manuscript to arXiv, Mikkelsen and Nakagawa, and Yu and coworkers independently submitted their own manuscripts to arXiv, presenting the same idea explored in this study. M. Mikkelsen, Y. O. Nakagawa, arXiv:2412.13839, 2024; J. Yu, et al, arXiv:2501.09721, 2025.
- [25] C. L. Cortes and S. K. Gray. Quantum Krylov subspace algorithms for ground- and excited-state energy estimation. *Phys. Rev. A*, 105:022417, 2022.
- [26] Z. Zhang, A. Wang, X. Xu, and Y. Li. Measurement-efficient quantum Krylov subspace diagonalization. *Quantum*, 8:1438, 2023.
- [27] O. Lockwood, P. Weiss, F. Aronshtein, and G. Verdon. Quantum dynamical Hamiltonian Monte Carlo. *Phys. Rev. Res.*, 6:033142, 2024.
- [28] A. A. Holmes, N. M. Tubman, and C. J. Umrigar. Heat-bath configuration interaction: an efficient selected configuration interaction algorithm inspired by heat-bath sampling. *J. Chem. Theory Comput.*, 12:3674–3680, 2016.
- [29] J. B. Schriber and F. A. Evangelista. An adaptive configuration interaction approach for strongly correlated electrons with tunable accuracy. *J. Chem. Phys.*, 144:161106, 2016.
- [30] P. M. Zimmerman. Incremental full configuration interaction. *J. Chem. Phys.*, 146:104102, 2017.
- [31] N. M. Tubman, C. Daniel Freeman, D. S. Levine, M. Head-Gordon, and K. Birgitta Whaley. Modern approaches to exact diagonalization and selected configuration interaction with the adaptive sampling CI method. *J. Chem. Theory Comput.*, 16:2139–2159, 2020.
- [32] P. Jordan and E. Wigner. Über das paulische äquivalenzverbot. *Z. Phys.*, 47:631–651, 1928.
- [33] H. F. Trotter. On the product of semi-groups of operators. *Proc. Am. Math. Soc.*, 10:545–551, 1959.
- [34] M. Suzuki. Relationship between d-dimensional quantum spin systems and (d + 1)-dimensional Ising systems: equivalence, critical exponents and systematic approximants of the partition function and spin correlations. *Prog. Theor. Phys.*, 56:1454–1469, 1976.
- [35] Y. Ouyang, D. R. White, and E. T. Campbell. Compilation by stochastic Hamiltonian sparsification. *Quantum*, 4:235, 2020.
- [36] H. Kurogi, K. Endo, Y. Sato, M. Sugawara, K. Wada, K. Sugisaki, S. Kanno, H. C. Watanabe, and H. Nakano. Optimizing a parameterized controlled gate with Free Quaternions Selection. arXiv:2409.13547, 2024.
- [37] J. Pipek and P. G. Mezey. A fast intrinsic localization procedure applicable for ab initio and semiempirical linear combination of atomic orbital wave functions. *J. Chem. Phys.*, 90:4916–4926, 1989.
- [38] G. M. J. Barca, C. Bertoni, L. Carrington, D. Datta, N. De Silva, J. Emiliano Deustua, D. G. Fedorov, J. R. Gour, A. O. Gunina, E. Guidez, T. Harville, S. Irle, J. Ivanic, K. Kowalski, S. S. Leang, H. Li, W. Li, J. J. Lutz, I. Magoulas, J. Mato, V. Mironov, H. Nakata, B. Q. Pham, P. Piecuch, D. Poole, S. R. Pruitt, A. P. Rendell, L. B. Roskop, K. Ruedenberg, T. Sattasathuchana, M. W. Schmidt, J. Shen, L. Slipchenko, M. Sosonkina, V. Sundriyal, A. Tiwari, J. L. Galvez Vallejo, B. Westheimer, M. Wloch, P. Xu, F. Zahariev, and M. S. Gordon. Recent developments in the general atomic and molecular electronic structure system. *J. Chem. Phys.*, 152:154102, 2020.
- [39] J. R. McClean, N. C. Rubin, K. J. Sung, I. D. Kivlichan, X. Bonet-Monroig, Y. Cao, C. Dai, E. Schuyler Fried, C. Gidney, B. Gimby, P. Gokhale, T. Häner, T. Hardikar, V. Havlíček, O. Higgott, C. Huang, J. Izaac, Z. Jiang, X. Liu, S. McArdle, M. Neeley, T. O’Brien, B. O’Gorman, I. Ozfidan, M. D. Radin, J. Romero, N. P. D. Sawaya, B. Senjean, K. Setia, S. Sim, D. S. Steiger, M. Steudtner, Q. Sun, W. Sun, D. Wang, F. Zhang, and R. Babbush. OpenFermion: the electronic structure package for quantum computers. *Quantum Sci. Technol.*, 5:034014, 2020.
- [40] M. J. Frisch, G. W. Trucks, H. B. Schlegel, G. E. Scuseria, M. A. Robb, J. R. Cheeseman, G. Scalmani, V. Barone, G. A. Petersson, H. Nakatsuji, X. Li, M. Caricato, A. V. Marenich, J. Bloino, B. G. Janesko, R. Gomperts, B. Mennucci, H. P. Hratchian, J. V. Ortiz, A. F. Izmaylov, J. L. Sonnenberg, D. Williams-Young, F. Ding, F. Lipparini, F. Egidi, J. Goings, B. Peng, A. Petrone, T. Henderson, D. Ranasinghe, V. G. Zakrzewski, J. Gao, N. Rega, G. Zheng, W. Liang, M. Hada, M. Ehara, K. Toyota, R. Fukuda, J. Hasegawa, M. Ishida, T. Nakajima, Y. Honda, O. Kitao, H. Nakai, T. Vreven, K. Throssell, J. A. Montgomery, Jr., J. E. Peralta, F. Ogliaro, M. J. Bearpark, J. J. Heyd, E. N. Brothers, K. N. Kudin, V. N. Staroverov, T. A. Keith, R. Kobayashi, J. Normand, K. Raghavachari, A. P. Ren-

- dell, J. C. Burant, S. S. Iyengar, J. Tomasi, M. Cossi, J. M. Millam, M. Klene, C. Adamo, R. Cammi, J. W. Ochterski, R. L. Martin, K. Morokuma, O. Farkas, J. B. Foresman, and D. J. Fox. Gaussian 16 Revision C.01, 2016. Gaussian Inc. Wallingford CT.
- [41] A. Tranter, P. J. Love, F. Mintert, and P. V. Coveney. A comparison of the Bravyi–Kitaev and Jordan–Wigner transformations for the quantum simulation of quantum chemistry. *J. Chem. Theory Comput.*, 14:5617–5630, 2018.
- [42] Quantum AI team and collaborators. qsim, September 2020.
- [43] M. Richer, G. Sánchez-Díaz, M. Martínez-González, V. Chuiko, T. D. Kim, A. Tehrani, S. Wang, P. B. Gaikwad, C. E. V. de Moura, C. Masschelein, R. A. Miranda-Quintana, A. Gerolin, F. Heider-Zadeh, and P. W. Ayers. PyCI: a python-scriptable library for arbitrary determinant CI. *J. Chem. Phys.*, 161:132502, 2024.
- [44] A. Ash Saki, S. Barison, B. Fuller, J. R. Garrison, J. R. Glick, C. Johnson, A. Mezzacapo, J. Robledo-Moreno, M. Rossmannek, P. Schweigert, I. Sitdikov, and K. J. Sung. Qiskit addon: sample-based quantum diagonalization. <https://github.com/Qiskit/qiskit-addon-sqd>, 2024.
- [45] Q. Sun, X. Zhang and S. Banerjee, P. Bao, M. Barbry, N. S. Blunt, N. A. Bogdanov, G. H. Booth, J. Chen, Z.-H. Cui, J. J. Eriksena dn Y. Gao, S. Guo, J. Hermann, M. R. Hermes, K. Koh, P. Koval, S. Lehtola, Z. Li, Z. Liu, N. Mardirossian, J. D. McClain, M. Motta, B. Mussard, H. Q. Pham, A. Pulkin, W. Purwanto, P. J. Robinson, E. Ronca, E. R. Sayfutyarova, M. Scheurer, H. F. Schurkus, J. E. T. Smith, C. Sun, S.-N. Sun, S. Upadhyay, L. K. Wagner, X. Wang, A. White, J. D. Whitfield, M. J. Williamson, S. Wouters, J. Yang, J. M. Yu, T. Zhu, T. C. Berkelbach, S. Sharma, A. Y. Sokolov, and G. K.-L. Chan. Recent developments in the PySCF program package. *J. Chem. Phys.*, 153:024109, 2020.
- [46] W. Zeng and J. Wu. Open-shell graphene fragments. *Chem*, 7:358–386, 2021.
- [47] A. J. Baldacchino, M. I. Collins, M. P. Nielsen, T. W. Schmidt, D. R. McCamey, and M. J. Y. Tayebjee. Singlet fission photovoltaics: Progress and promising pathways. *Chem. Phys. Rev.*, 3:021304, 2022.
- [48] B. Singh and J. S. Brinen. Low-temperature photochemistry of *p*-diazidobenzene and 4,4'-diazidoazobenzene. *J. Am. Chem. Soc.*, 93:540–542, 1971.
- [49] A. Nicolaides, H. Tomioka, and S. Murata. Direct observation and characterization of *p*-phenylenebisnitrene. a labile quinoidal diradical. *J. Am. Chem. Soc.*, 120:11530–11531, 1998.
- [50] S. Nimura, O. Kikuchi, T. Ohana, A. Yabe, and M. Kaise. Singlet-triplet energy gaps of quinonoidal dinitrenes. *Chem. Lett.*, 25:125–126, 2016.
- [51] A. S. Ichimura, K. Sato, T. Kinoshita, T. Takui, K. Itoh, and P. M. Lahti. An electron spin resonance study of persistent dinitrenes. *Mol. Cryst. Liq. Cryst.*, 271/272:279–288, 1995.
- [52] K. Sugisaki, K. Toyota, K. Sato, D. Shiomi, M. Kitagawa, and T. Takui. Quantum chemical calculations of the zero-field splitting tensors for organic spin multiplets. In A. Lund and M. Shiotani, editors, *EPR of Free Radicals in Solids I: Trends in Methods and Applications*, 2nd Edition, pages 363–392. Springer, Dordrecht, 2013.
- [53] M. Liu, V. I. Artyukhov, H. Lee, F. Xu, and B. I. Yakobson. Carbyne from first principles; chain of C atoms, a nanorod or a nanorope. *ACS Nano*, 7:10075–10082, 2013.
- [54] M. Liu, V. I. Artyukhov, H. Lee, F. Xu, and B. I. Yakobson. Correction to carbyne from first principles; chain of C atoms, a nanorod or a nanorope. *ACS Nano*, 11:5186, 2017.
- [55] H. Gao, S. Imamura, A. Kasagi, and E. Yoshida. Distributed implementation of full configuration interaction for one trillion determinants. *J. Chem. Theory Comput.*, 20:1185–1192, 2024.
- [56] P. Reinholdt, K. M. Ziems, E. R. Kjellgren, S. Coriani, S. P. A. Sauer, and J. Kongsted. Exposing a fatal flaw in sample-based quantum diagonalization methods. arXiv:2501.07231, 2025.
- [57] Y. Yoshida, L. Erhart, T. Murokoshi, R. Nakagawa, C. Mori, T. Miyanaga, T. Mori, and W. Mizukami. Auxiliary-field quantum Monte Carlo method with quantum selected configuration interaction. arXiv:2502.21081, 2025.
- [58] D. Danilov, J. Robledo-Moreno, K. J. Sung, M. Motta, and J. Shee. Enhancing the accuracy and efficiency of sample-based quantum diagonalization with phaseless auxiliary-field quantum Monte Carlo. arXiv:2503.05967.

S1. SUPPORTING INFORMATION

A. Active spaces

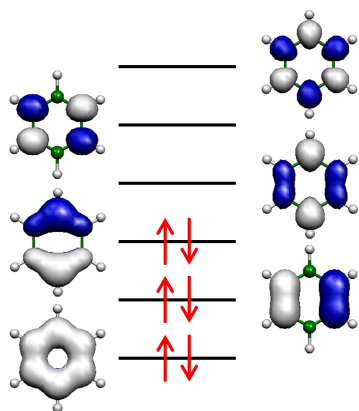


FIG. S1. (6e,6o) active orbitals of **1**. Red arrows specify the electron occupancy in the RHF configuration.

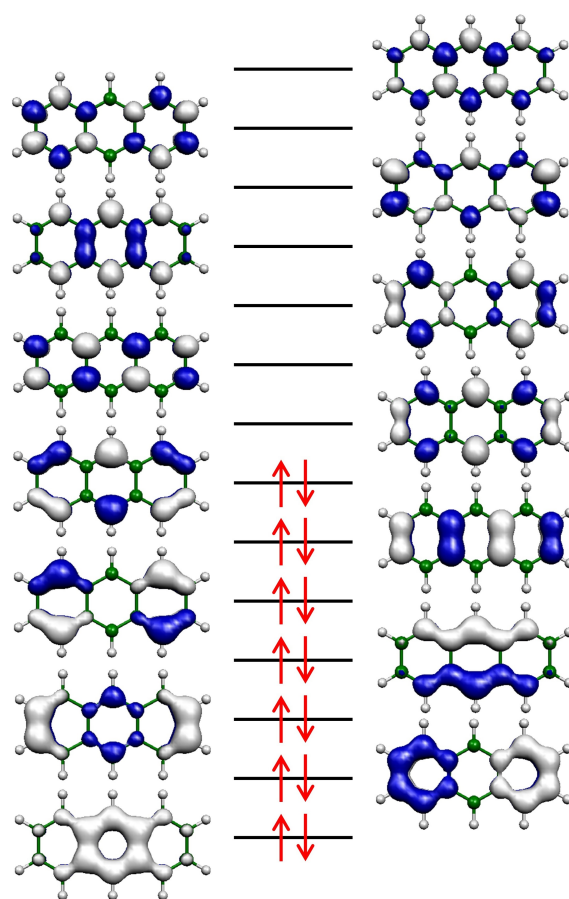


FIG. S3. (14e,14o) active space of **3**. Red arrows specify the electron occupancy in the RHF configuration.

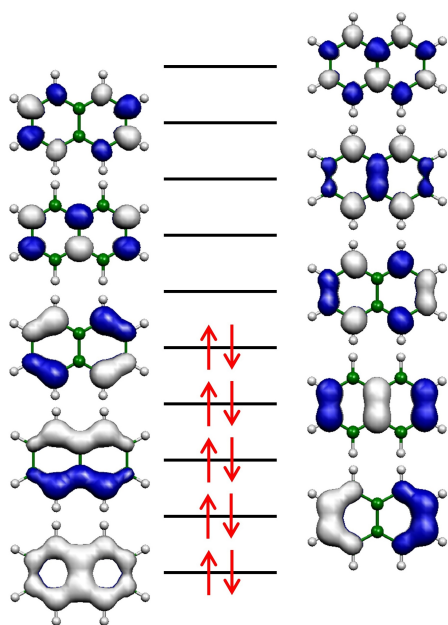


FIG. S2. (10e,10o) active space of **2**. Red arrows specify the electron occupancy in the RHF configuration.

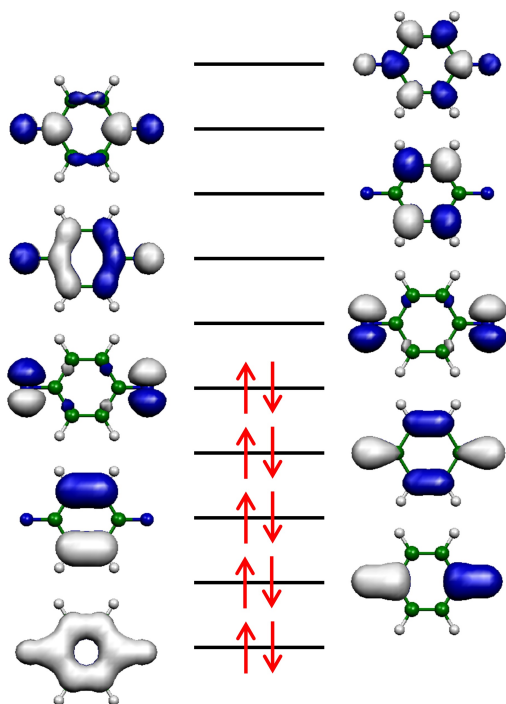


FIG. S4. (10e,10o) active space of **4**. Red arrows specify the electron occupancy in the RHF configuration.

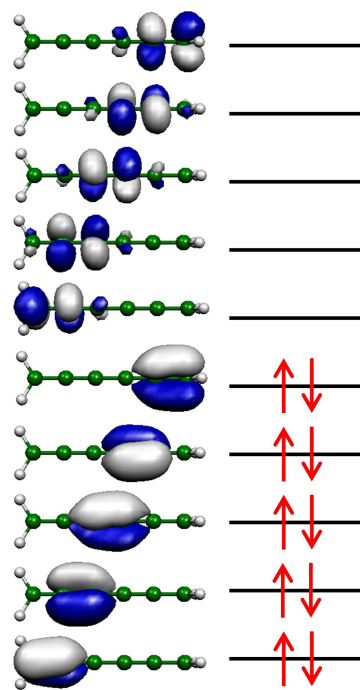


FIG. S6. (10e,10o) active space of **5** in twisted geometry. Red arrows specify the electron occupancy in the RHF configuration.

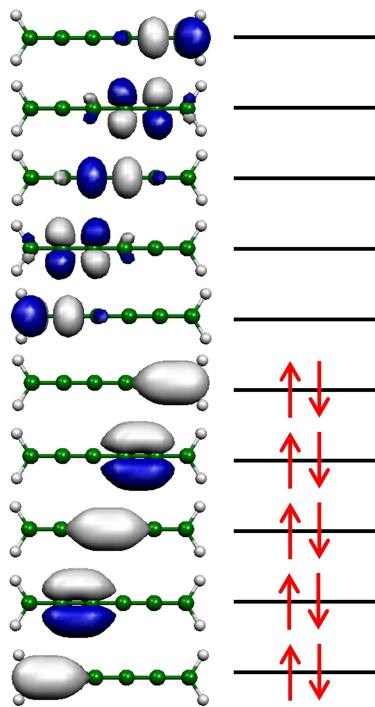


FIG. S5. (10e,10o) active space of **5** in planar geometry. Red arrows specify the electron occupancy in the RHF configuration.

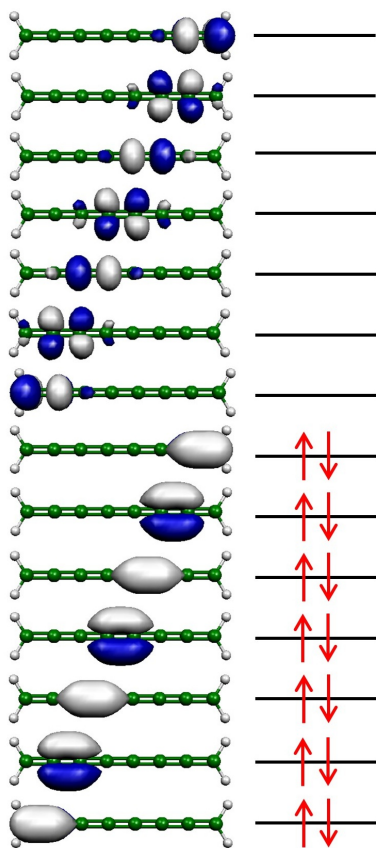


FIG. S7. (14e,14o) active space of **6** in planar geometry. Red arrows specify the electron occupancy in the RHF configuration.

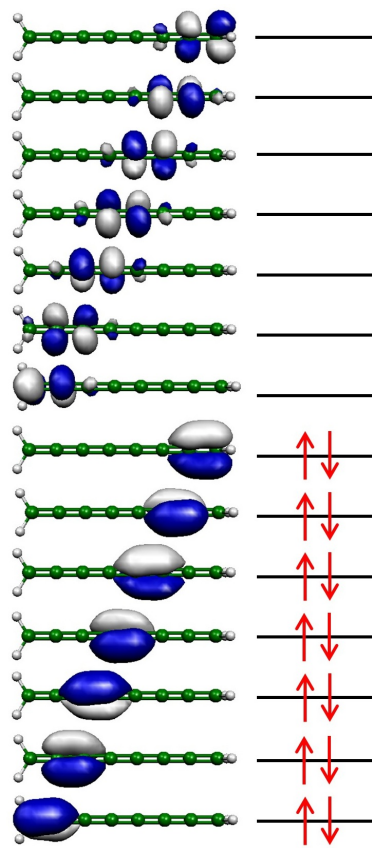


FIG. S8. (14e,14o) active space of **6** in twisted geometry. Red arrows specify the electron occupancy in the RHF configuration.

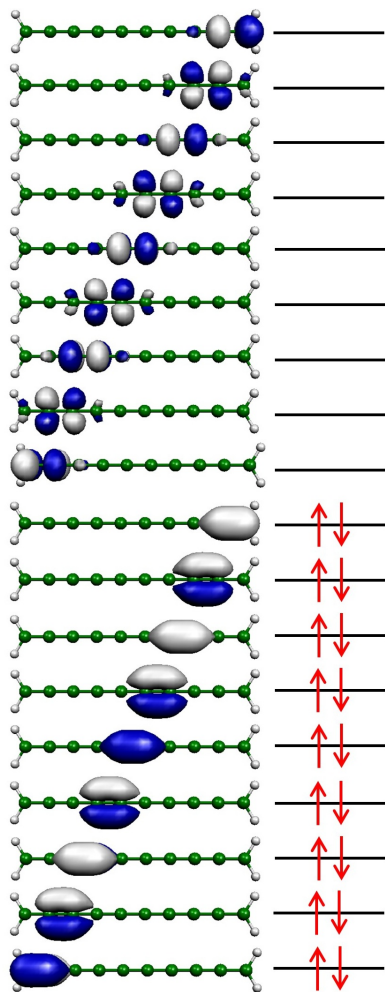


FIG. S9. (18e,18o) active space of **7** in planar geometry. Red arrows specify the electron occupancy in the RHF configuration.

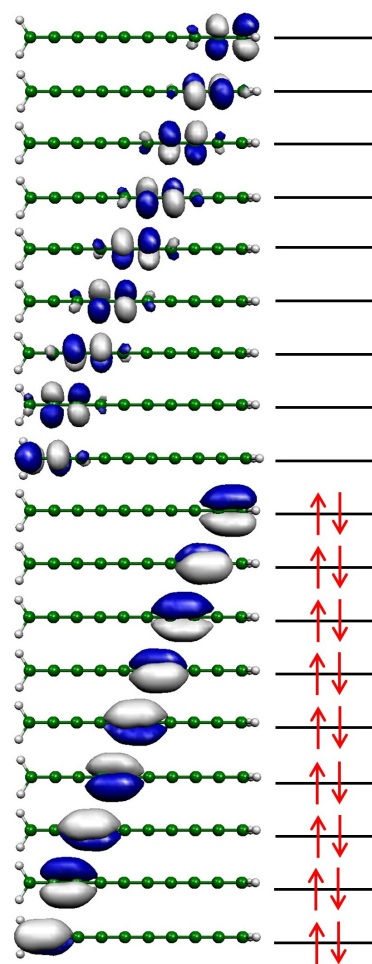


FIG. S10. (18e,18o) active space of **7** in twisted geometry. Red arrows specify the electron occupancy in the RHF configuration.

B. Cartesian coordinates

TABLE S1. Cartesian coordinates of the B3LYP/6-31G* optimized geometry of **1**, in units of Å.

Atom	X	Y	Z
C	0.000000	1.396602	0.000000
C	0.000000	-1.396602	0.000000
C	1.209493	0.698301	0.000000
C	1.209493	-0.698301	0.000000
C	-1.209493	0.698301	0.000000
C	-1.209493	-0.698301	0.000000
H	0.000000	2.483720	0.000000
H	0.000000	-2.483720	0.000000
H	2.150965	1.241860	0.000000
H	2.150965	-1.241860	0.000000
H	-2.150965	1.241860	0.000000
H	-2.150965	-1.241860	0.000000

TABLE S2. Cartesian coordinates of the B3LYP/6-31G* optimized geometry of **2**, in units of Å.

Atom	X	Y	Z
C	0.000000	0.000000	0.717063
C	0.000000	0.000000	-0.717063
C	0.000000	1.244791	1.402547
C	0.000000	1.244791	-1.402547
C	0.000000	-1.244791	1.402547
C	0.000000	-1.244791	-1.402547
C	0.000000	2.433546	0.708438
C	0.000000	2.433546	-0.708438
C	0.000000	-2.433546	0.708438
C	0.000000	-2.433546	-0.708438
H	0.000000	1.242227	2.490221
H	0.000000	1.242227	-2.490221
H	0.000000	-1.242227	2.490221
H	0.000000	-1.242227	-2.490221
H	0.000000	3.378258	1.245514
H	0.000000	3.378258	-1.245514
H	0.000000	-3.378258	1.245514
H	0.000000	-3.378258	-1.245514

TABLE S3. Cartesian coordinates of the B3LYP/6-31G* optimized geometry of **3**, in units of Å.

Atom	X	Y	Z
C	0.000000	0.000000	1.403608
C	0.000000	0.000000	-1.403608
C	0.000000	1.223844	0.722822
C	0.000000	1.223844	-0.722822
C	0.000000	-1.223844	0.722822
C	0.000000	-1.223844	-0.722822
C	0.000000	2.479411	1.407056
C	0.000000	2.479411	-1.407056
C	0.000000	-2.479411	1.407056
C	0.000000	-2.479411	-1.407056
C	0.000000	3.660505	0.713049
C	0.000000	3.660505	-0.713049
C	0.000000	-3.660505	0.713049
C	0.000000	-3.660505	-0.713049
H	0.000000	0.000000	2.491948
H	0.000000	0.000000	-2.491948
H	0.000000	2.477069	2.494589
H	0.000000	2.477069	-2.494589
H	0.000000	-2.477069	2.494589
H	0.000000	-2.477069	-2.494589
H	0.000000	4.607098	1.246673
H	0.000000	4.607098	-1.246673
H	0.000000	-4.607098	1.246673
H	0.000000	-4.607098	-1.246673

TABLE S4. Cartesian coordinates of the CASSCF(10e,10o)/6-31G* optimized geometry of **4**, in units of Å.

Atom	X	Y	Z
C	0.000000	0.000000	1.429275
C	0.000000	0.000000	-1.429275
C	0.000000	1.259487	0.674849
C	0.000000	1.259487	-0.674849
C	0.000000	-1.259487	0.674849
C	0.000000	-1.259487	-0.674849
N	0.000000	0.000000	2.710369
N	0.000000	0.000000	-2.710369
H	0.000000	2.176735	1.233246
H	0.000000	2.176735	-1.233246
H	0.000000	-2.176735	1.233246
H	0.000000	-2.176735	-1.233246

TABLE S5. Cartesian coordinates of the planar geometry of **5** optimized at the B3LYP/6-31G* level, in units of Å.

Atom	X	Y	Z
C	0.000000	0.000000	3.236615
C	0.000000	0.000000	1.918246
C	0.000000	0.000000	0.645266
C	0.000000	0.000000	-0.645266
C	0.000000	0.000000	-1.918246
C	0.000000	0.000000	-3.236615
H	0.000000	0.927096	3.807401
H	0.000000	0.927096	-3.807401
H	0.000000	-0.927096	3.807401
H	0.000000	-0.927096	-3.807401

TABLE S6. Cartesian coordinates of the twisted geometry of **5**, in units of Å.

Atom	X	Y	Z
C	0.000000	0.000000	3.236615
C	0.000000	0.000000	1.918246
C	0.000000	0.000000	0.645266
C	0.000000	0.000000	-0.645266
C	0.000000	0.000000	-1.918246
C	0.000000	0.000000	-3.236615
H	0.000000	0.927096	3.807401
H	0.927096	0.000000	-3.807401
H	0.000000	-0.927096	3.807401
H	-0.927096	0.000000	-3.807401

TABLE S7. Cartesian coordinates of the planar geometry of **6** optimized at the B3LYP/6-31G* level, in units of Å.

Atom	X	Y	Z
C	0.000000	0.000000	4.519296
C	0.000000	0.000000	3.200579
C	0.000000	0.000000	1.926668
C	0.000000	0.000000	0.637785
C	0.000000	0.000000	-0.637785
C	0.000000	0.000000	-1.926668
C	0.000000	0.000000	-3.200579
C	0.000000	0.000000	-4.519296
H	0.000000	0.927134	5.090044
H	0.000000	0.927134	-5.090044
H	0.000000	-0.927134	5.090044
H	0.000000	-0.927134	-5.090044

TABLE S8. Cartesian coordinates of the twisted geometry of **6**, in units of Å.

Atom	X	Y	Z
C	0.000000	0.000000	4.519296
C	0.000000	0.000000	3.200579
C	0.000000	0.000000	1.926668
C	0.000000	0.000000	0.637785
C	0.000000	0.000000	-0.637785
C	0.000000	0.000000	-1.926668
C	0.000000	0.000000	-3.200579
C	0.000000	0.000000	-4.519296
H	0.000000	0.927134	5.090044
H	0.927134	0.000000	-5.090044
H	0.000000	-0.927134	5.090044
H	-0.927134	0.000000	-5.090044

TABLE S9. Cartesian coordinates of the planar geometry of **7** optimized at the B3LYP/6-31G* level, in units of Å.

Atom	X	Y	Z
C	0.000000	0.000000	5.801617
C	0.000000	0.000000	4.482729
C	0.000000	0.000000	3.208380
C	0.000000	0.000000	1.920044
C	0.000000	0.000000	0.643194
C	0.000000	0.000000	-0.643194
C	0.000000	0.000000	-1.920044
C	0.000000	0.000000	-3.208380
C	0.000000	0.000000	-4.482729
C	0.000000	0.000000	-5.801617
H	0.000000	0.927308	6.372154
H	0.000000	0.927308	-6.372154
H	0.000000	-0.927308	6.372154
H	0.000000	-0.927308	-6.372154

TABLE S10. Cartesian coordinates of the twisted geometry of **7**, in units of Å.

Atom	X	Y	Z
C	0.000000	0.000000	5.801617
C	0.000000	0.000000	4.482729
C	0.000000	0.000000	3.208380
C	0.000000	0.000000	1.920044
C	0.000000	0.000000	0.643194
C	0.000000	0.000000	-0.643194
C	0.000000	0.000000	-1.920044
C	0.000000	0.000000	-3.208380
C	0.000000	0.000000	-4.482729
C	0.000000	0.000000	-5.801617
H	0.000000	0.927308	6.372154
H	0.927308	0.000000	-6.372154
H	0.000000	-0.927308	6.372154
H	-0.927308	0.000000	-6.372154

C. The CAS-CI wave function

TABLE S11. CAS-CI(6e,6o)/STO-3G wave function of the S_0 state of **1**. Only the Slater determinants having the coefficients larger than 0.05 in absolute value are listed.

Alpha	Beta	Coefficients
111000	111000	0.9166
110100	110100	-0.1733
101010	101010	-0.1733
110010	101100	-0.1153
101100	110010	-0.1153
111000	100110	0.0829
100110	111000	0.0829
110001	011100	0.0776
011100	110001	0.0776
101001	011010	0.0776
011010	101001	0.0776
101010	101001	0.0558
011001	101010	0.0558
110100	011001	0.0558
011001	110100	0.0558

TABLE S12. CAS-CI(6e,6o)/STO-3G wave function of the T_1 state of **1**. Only the Slater determinants having the coefficients larger than 0.05 in absolute value are listed.

Alpha	Beta	Coefficients
111100	110000	0.6456
111010	101000	0.6456
111001	011000	-0.2225
101110	100010	-0.1341
110110	100100	-0.1341
011110	100001	0.0872
110101	010100	0.0811
101011	001010	0.0811
101101	010010	0.0795
110011	001100	0.0795
111100	010100	0.0577
111010	010010	-0.0577
111100	001010	-0.0577
111010	001100	-0.0577
110101	110000	0.0573
101101	101000	-0.0573
101011	110000	-0.0573
110011	101000	-0.0573

TABLE S14. CAS-CI(10e,10o)/STO-3G wave function of the T_1 state of **2**. Only the Slater determinants having the coefficients larger than 0.05 in absolute value are listed.

Alpha	Beta	Coefficients
1111110000	1111000000	0.7111
1111101000	1110100000	-0.3703
1111100100	1101100000	0.2860
1111100010	1011100000	0.1859
1111100001	0111100000	-0.1176
1110111000	1110001000	-0.1101
1111010100	1101010000	-0.1016
1111011000	1110010000	0.0952
1110110100	1101001000	0.0840
1101110100	1101000100	-0.0770
1111010010	1011100000	-0.0715
1101111000	1110000100	0.0690
1110110010	1011001000	0.0668
1011111000	1110000010	0.0637
1111110000	1101001000	0.0599
1110110100	1111000000	0.0583
1110101100	1100101000	-0.0556
1111110000	1011010000	-0.0555
1111001100	1100110000	0.0551
1111010010	1111000000	0.0542
1110101010	1010101000	-0.0535
1111101000	1011001000	0.0511
1110110010	1110100000	-0.0505
1011110010	1011000010	-0.0503

TABLE S13. CAS-CI(10e,10o)/STO-3G wave function of the S_0 state of **2**. Only the Slater determinants having the coefficients larger than 0.05 in absolute value are listed.

Alpha	Beta	Coefficients
1111100000	1111100000	0.8615
1111010000	1111010000	-0.1498
1110101000	1110101000	-0.1338
1111001000	1110110000	0.0973
1110110000	1111001000	0.0973
1111000100	1101110000	-0.0856
1101110000	1111000100	-0.0856
1111010000	1101100100	-0.0780
1101100100	1111010000	-0.0780
1111100000	1110011000	-0.0735
1110011000	1111100000	-0.0735
1110100100	1101101000	0.0706
1101101000	1110100100	0.0706
1111000010	1011110000	-0.0692
1011110000	1111000010	-0.0692
1101100100	1101100100	-0.0671
1101110000	1101110000	-0.0652
1111000100	1111000100	-0.0625
1110100010	1011101000	0.0587
1011101000	1110100010	0.0587
1110100001	0111101000	-0.0501
0111101000	1110100001	-0.0501

TABLE S15. CAS-CI(14e,14o)/STO-3G wave function of the S_0 state of **3**. Only the Slater determinants having the coefficients larger than 0.05 in absolute value are listed.

Alpha	Beta	Coefficients
11111110000000	11111110000000	0.8021
11111101000000	11111101000000	-0.1588
11111010100000	11111010100000	-0.1066
11111100100000	11111100100000	0.0891
11111011000000	11111011000000	0.0891
11110110010000	11110110010000	-0.0741
11111100010000	11110111000000	-0.0719
11110111000000	11111100010000	-0.0719
11111110000000	11111001100000	-0.0681
11111001100000	11111110000000	-0.0681
11111100001000	11101111000000	0.0673
11101111000000	11111100001000	0.0673
11111100000100	11011111000000	-0.0627
11011111000000	11111100000100	-0.0627
11111101000000	11110110010000	-0.0617
11110110010000	11111101000000	-0.0617
11111101000000	11101110001000	0.0579
11101110001000	11111101000000	0.0579
11110100100000	11110110100000	0.0552
11110110100000	11110100100000	0.0552
11111010001000	11101110100000	-0.0514
11101110100000	11111010001000	-0.0514

TABLE S16. CAS-CI(14e,14o)/STO-3G wave function of the T_1 state of **3**. Only the Slater determinants having the coefficients larger than 0.05 in absolute value are listed.

Alpha	Beta	Coefficients
1111111000000	11111100000000	0.7043
11111110010000	11110110000000	0.2348
11111110100000	11111010000000	-0.2284
11111110001000	11101110000000	-0.1778
11111110000100	11011110000000	0.1439
11111011100000	11111000100000	-0.0886
11111110000010	10111110000000	0.0886
11111101010000	11110101000000	-0.0865
11111110000001	01111110000000	0.0771
11110111010000	11110100010000	-0.0767
11111110100000	11111001000000	0.0749
11111011010000	11110100100000	0.0722
11111101001000	11101101000000	0.0688
11111101000100	11011101000000	-0.0634
11111111000000	11011101000000	-0.0598
111111010000100	11111100000000	0.0584
11111111000000	11110100100000	-0.0581
1111111100001000	11111100000000	0.0581
11111111000000	11101110000000	-0.0581
111110110000100	11011100100000	0.0571
11111011010000	11111100000000	-0.0562
11110111100000	11111000010000	0.0542
11111011001000	11101100100000	-0.0533
11011111100000	11111000000100	0.0503

TABLE S17. CAS-CI(10e,10o)/6-31G* wave function of the S_0 state of **4**. Only the Slater determinants having the coefficients larger than 0.05 in absolute value are listed.

Alpha	Beta	Coefficients
1111100000	1111100000	0.6291
1111010000	1111010000	-0.6134
1110101000	1110101000	-0.1358
1110011000	1110011000	0.1346
1111001000	1110110000	0.0926
1110110000	1111001000	0.0926
1101100100	1101100100	-0.0788
1101010100	1101010100	0.0769
1110100010	1011101000	-0.0666
1011101000	1110100010	-0.0666
1110010010	1011011000	0.0653
1011011000	1110010010	0.0653
1011100010	1011100010	-0.0542
1011010010	1011010010	0.0531
1101100100	1110101000	-0.0513
1110101000	1101100100	-0.0513
1110100100	1101101000	-0.0510
1101101000	1110100100	-0.0510
1110011000	1101010100	0.0504
1101010100	1110011000	0.0504

TABLE S18. CAS-CI(10e,10o)/6-31G* wave function of the T_1 state of **4**. Only the Slater determinants having the coefficients larger than 0.05 in absolute value are listed.

Alpha	Beta	Coefficients
1111110000	1111000000	0.8848
1110111000	1110001000	-0.1835
1101110100	1101000100	-0.1105
1011111000	1110000010	-0.0967
1110110010	1011001000	0.0891
1111101000	1110100000	-0.0840
1111011000	1110010000	0.0824
1101111000	1110000100	-0.0758
1011110010	1011000010	-0.0742
1101110100	1110001000	-0.0718
1110110100	1101001000	-0.0718
1011111000	1101001000	-0.0671
1011110010	1110001000	-0.0670
1011110010	1110001000	-0.0644
1110111000	1011000010	-0.0633
0111111000	1110000001	-0.0554
1101111000	1101001000	-0.0525
1110110001	0111001000	-0.0500

TABLE S19. CAS-CI(10e,10o)/6-31G* wave function of the S_0 state of **5** in planar geometry. Only the Slater determinants having the coefficients larger than 0.05 in absolute value are listed.

Alpha	Beta	Coefficients
1111100000	1111100000	0.8943
1111000001	1111000001	-0.1638
0111110000	0111110000	-0.1638
1101100100	1101100100	-0.1349
1011101000	1011101000	-0.1266
1110100010	1110100010	-0.1266
1101100001	1111000100	0.0503
1111000100	1101100001	0.0503
0111100100	1101110000	-0.0503
1101110000	0111100100	-0.0503

TABLE S20. CAS-CI(10e,10o)/6-31G* wave function of the T_1 state of **5** in planar geometry. Only the Slater determinants having the coefficients larger than 0.05 in absolute value are listed.

Alpha	Beta	Coefficients
1111100100	1101100000	0.4112
1111110000	0111100000	0.3648
1111100001	1111000000	-0.3648
1111100100	1111000000	-0.2693
1111100100	0111100000	-0.2693
1111110000	1101100000	-0.2677
1111100001	1101100000	0.2677
1111110000	1111000000	0.1912
1111100001	0111100000	-0.1912
1111100100	1101000001	0.0651
1111100100	0101110000	-0.0651
1111000101	1101000001	0.0643
0111110100	0101110000	0.0643
1111100001	1101000100	0.0635
1111110000	0101100100	-0.0635
1111010001	0111000001	0.0621
0111110001	0111010000	-0.0621
1011101100	1001101000	0.0585
1110100110	1100100010	0.0585
1101100101	1111000000	0.0569
1101110100	0111100000	-0.0569
1111000101	1101100000	0.0554
0111110100	1101100000	-0.0554
1111110000	0111000100	0.0528
1111100001	0111000100	-0.0528
1111100001	0111010000	0.0518
1111110000	0111000001	0.0518
1110110010	0110100010	0.0512
1011101001	1011001000	-0.0512
1111100001	1101000001	0.0508
1111110000	0101110000	0.0508
1011111000	0011101000	0.0503
1110100011	1110000010	-0.0503

TABLE S22. CAS-CI(10e,10o)/6-31G* wave function of the T_1 state of **5** in twisted geometry. Only the Slater determinants having the coefficients larger than 0.05 in absolute value are listed.

Alpha	Beta	Coefficients
1111100100	1101100000	0.3522
1111100001	1111000000	0.2650
1111110000	0111100000	-0.2650
1111100100	1111000000	-0.2209
1111100100	0111100000	-0.2209
1111100001	1101100000	-0.2074
1111110000	1101100000	0.2074
1111100100	1011100000	0.1938
1111100100	1110100000	0.1938
1111100010	1110100000	-0.1625
1111101000	1011100000	0.1625
1111110000	1011100000	0.1498
1111100001	1110100000	-0.1498
1111100010	1101100000	-0.1471
1111101000	1101100000	0.1471
1111100001	0111100000	0.1437
1111110000	1111000000	-0.1437
1111100001	1011100000	-0.1228
1111110000	1110100000	0.1228
1111100010	1111000000	0.1221
1111101000	0111100000	-0.1221
1111100010	1011100000	-0.1088
1111101000	1110100000	0.1088
1111100010	0111100000	0.0962
1111101000	1111000000	-0.0962
1111000101	1101000001	0.0562
0111110100	0101110000	0.0562
1011101100	1001101000	0.0513
1110100110	1100100010	0.0513
1111100100	0101110000	-0.0511
1111100100	1101000001	0.0511

TABLE S21. CAS-CI(10e,10o)/6-31G* wave function of the S_0 state of **5** in twisted geometry. Only the Slater determinants having the coefficients larger than 0.05 in absolute value are listed.

Alpha	Beta	Coefficients
1111100000	1111100000	0.8519
1111000001	1111000001	-0.1630
0111110000	0111110000	-0.1630
1101100100	1101100100	-0.1431
1011101000	1011101000	-0.1295
1110100010	1110100010	-0.1295
1101110000	0111110010	0.0618
0111110010	1101110000	0.0618
1111000100	1101100001	-0.0618
1101100001	1111000100	-0.0618

D. HSB-QSCI results calculated using `kernel_fixed_space` subroutine in PySCF

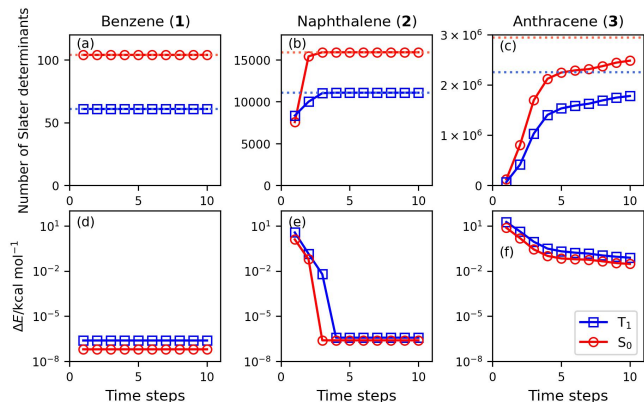


FIG. S11. HSB-QSCI results of oligoacenes, calculated using `kernel_fixed_space` subroutine in PySCF. The number of Slater determinants included in the Hamiltonian diagonalization is given in (a), (b), and (c) for **1**, **2**, and **3**, respectively. Red and blue indicate the spin-singlet ground and spin-triplet excited states, respectively. Dotted lines represent the number of Slater determinants in the CAS-CI wave function. The difference of the HSB-QSCI energy from the CAS-CI values in units of kcal mol^{-1} are given in (d), (e), and (f) on the logarithmic scale.

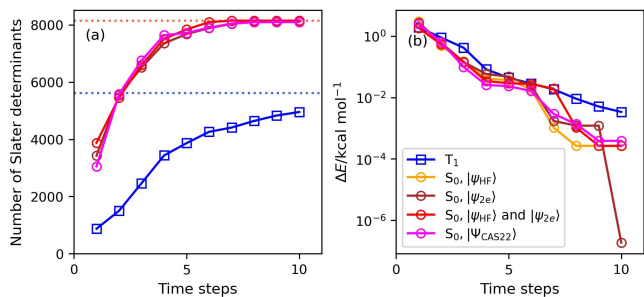


FIG. S12. HSB-QSCI results of **4**, calculated using `kernel_fixed_space` subroutine in PySCF. (a) The number of Slater determinants sampled from Hamiltonian simulations. The red and blue dotted lines indicate the number of Slater determinants in the CAS-CI wave function. (b) The difference of the HSB-QSCI energy from the CAS-CI values in units of kcal mol^{-1} , on the logarithmic scale.

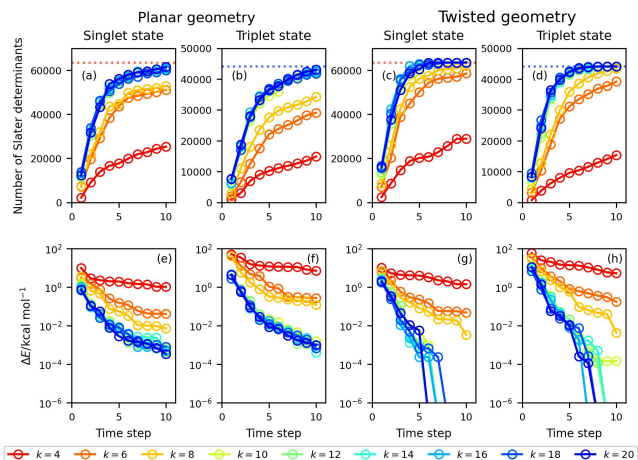


FIG. S13. HSB-QSCI results of **5** in its planar and twisted geometries with different maximum locality values, calculated using `kernel_fixed_space` subroutine in PySCF. The number of Slater determinants included in the Hamiltonian diagonalization is given in (a), (b), (c), and (d). The red and blue dotted lines represent the number of Slater determinants in the CAS-CI wave function of the S₀ and T₁ states, respectively. The difference of the HSB-QSCI energy from the CAS-CI values in units of kcal mol^{-1} are given in (e), (f), (g), and (h) on the logarithmic scale.

E. Shot number dependence on the HSB-QSCI simulations of **3**

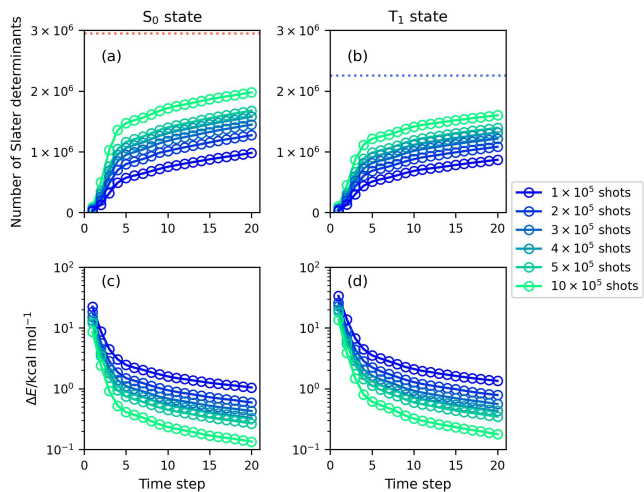


FIG. S14. Shot number and time step dependence on the HSB-QSCI simulations of **3**. The number of Slater determinants sampled from Hamiltonian simulations is plotted in (a) and (b) for the S₀ and T₁ states, respectively. The red and blue dotted lines indicate the number of Slater determinants in the CAS-CI wave function. (b) The difference of the HSB-QSCI energy from the CAS-CI values in units of kcal mol^{-1} , in log scale is given in (c) and (d) for the S₀ and T₁ states, respectively.

F. Shot number dependence on the HSB-QSCI simulations of $\mathbf{5}$ with the maximum locality $m = 6$

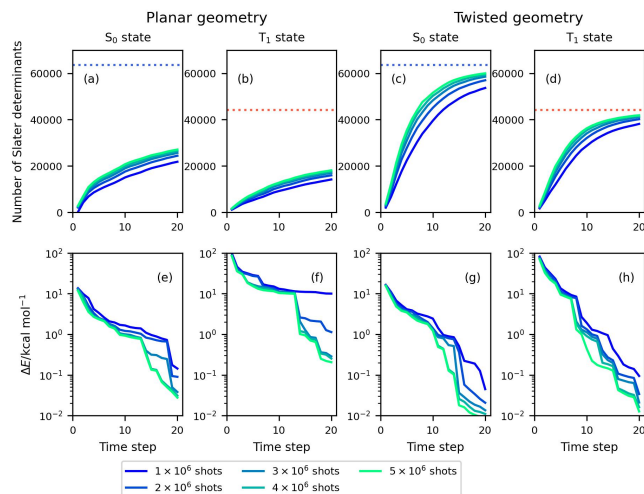


FIG. S15. Shot number and time step dependence on the HSB-QSCI simulations of $\mathbf{5}$ in its planar and twisted geometries with the maximum locality of Hamiltonian terms $m = 6$. The number of Slater determinants included in the Hamiltonian diagonalization is given in (a), (b), (c), and (d). The red and blue dotted lines represent the number of Slater determinants in the CAS-CI wave function of the S_0 and T_1 states, respectively. The difference of the HSB-QSCI energy from the CAS-CI values in units of kcal mol^{-1} are given in (e), (f), (g), and (h) on the logarithmic scale.